Tectonophysics 824 (2022) 229221

Contents lists available at ScienceDirect

Tectonophysics

journal homepage: www.elsevier.com/locate/tecto

Dynamic compressive strength and fragmentation in sedimentary and metamorphic rocks

Auriol S.P. Rae [a,b,*], Thomas Kenkmann [a], Vivek Padmanabha [a,c], Michael H. Poelchau [a], Frank Schäfer [a,c], Matthias A. Dörfler [c], Louis Müller [a]

[a] Institute of Earth and Environmental Sciences – Geology, Albert-Ludwigs Universität Freiburg, Albertstrasse 23b, 79104 Freiburg, Germany
[b] Department of Earth Sciences, University of Cambridge, Cambridge CB2 3EQ, UK
[c] Fraunhofer Institute for High-Speed Dynamics, Ernst-Mach-Institut (EMI), Ernst-Zermelo-strasse 4, 79104 Freiburg, Germany.

ARTICLE INFO

Keywords:
Dynamic failure
Strength
Strain rate
Fragmentation
Pulverised fault rocks
Brittle deformation

ABSTRACT

Brittle deformation at high strain rates results in intense fragmentation and rock pulverisation. For rocks, the critical strain rate at which this behaviour occurs is ~10^2 s^{-1}. The mechanical properties of rocks at these strain rates can also be very different from their quasi-static properties. Deformation of rocks at these strain rates can occur during fault rupture, landslide events, and meteorite impacts. In this study, we present the results of high strain rate mechanical tests to determine the characteristic strain rate for rate-dependent brittle failure, and the fragment size and shape distributions that result from failure at these conditions. We investigated sandstone, quartzite, limestone, and marble and considered whether the fragment characteristics can be used as diagnostic indicators of loading conditions during brittle failure. We find that the characteristic strain rates, where the dynamic strength is twice the quasi-static strength, range between ~150 and 300 s^{-1} for rate-dependent brittle failure in the investigated lithologies. Furthermore, we use our results to demonstrate an empirical inverse power-law relationship between fragment size and strain rate for dynamic failure under uniaxial compression. On the other hand, we show that fragment shape is independent of strain rate under dynamic uniaxial loading.

1. Introduction

Fragmentation of rocks occurs during a variety of geological processes, including seismogenic fault rupture (e.g., Aben et al., 2017), gravitational mass movements (e.g., De Blasio and Crosta, 2014), and meteorite impacts (e.g., Kenkmann et al., 2014). In all these events, brittle failure may occur under dynamic, high strain rate conditions. At these conditions, the mechanical properties of rocks (Zhang and Zhao, 2014), the behaviour of individual fractures (Fineberg et al., 1991; Ravi-Chandar and Knauss, 1984a; Sharon and Fineberg, 1999; Zhang et al., 1999), and the interaction between growing fractures (e.g., Ramesh et al., 2015) can be strongly rate-dependent and deviate from quasi-static brittle failure.

The results of mechanical experiments demonstrate that rocks behave with a strength that is near constant at low strain rates before increasing markedly beyond a threshold strain rate of ~10^0–10^3 s^{-1} (Aben et al., 2017; Ramesh et al., 2015; Zhang and Zhao, 2014, and refs. therein). A number of analytical and micromechanical models have been developed that demonstrate this increase in strength (Bhat et al., 2012; Hild et al., 2003; Paliwal and Ramesh, 2008). Based on a study that explored one of these micromechanical models (Paliwal and Ramesh, 2008), Kimberley et al. (2013) demonstrated that the behaviour of rocks from quasi-static to high strain rates can be described by a universal scaling relationship:

$$\frac{\sigma_c}{\sigma_0} = 1 + \frac{\dot{\varepsilon}^{\frac{2}{3}}}{\dot{\varepsilon}_0} \quad (1)$$

where σ_c and $\dot{\varepsilon}$ are the compressive strength and strain rate, respectively, and the material parameters, σ_0 and $\dot{\varepsilon}_0$, are the characteristic strength and characteristic strain rate, respectively. The characteristic strength is equivalent to the quasi-static uniaxial compressive strength and the characteristic strain rate corresponds to the strain rate at which strength is double the value of the quasi-static strength.

The dependence of rock strength on strain rate is fundamentally linked to the nucleation and growth of fractures. Fractures propagate at a finite velocity: during failure at low rates, the weakest available flaw in

* Corresponding author at: Department of Earth Sciences, University of Cambridge, Cambridge CB2 3EQ, UK.
E-mail address: aspr2@cam.ac.uk (A.S.P. Rae).

https://doi.org/10.1016/j.tecto.2022.229221
Received 14 August 2021; Received in revised form 4 January 2022; Accepted 7 January 2022
Available online 19 January 2022
0040-1951/© 2022 The Authors. Published by Elsevier B.V. This is an open access article under the CC BY license (http://creativecommons.org/licenses/by/4.0/).

a material can initiate a single fracture that can grow fast enough to accommodate the applied loading; at high rates, that single flaw cannot develop a single fracture before other increasingly strong flaws are activated (Aben et al., 2017; Ramesh et al., 2015). Furthermore, it has been demonstrated that the behaviour of individual fractures may change as a result of high-rate loading by increasing the fracture toughness and producing hierarchical fracture branches (Ravi-Chandar and Knauss, 1984a; Sharon and Fineberg, 1999; Zhang et al., 1999). The consequence of these processes is that rock failure at high strain rates leads to intense fracturing and fragmentation.

Upper crustal fault zones generally consist of a fault core and a surrounding damage zone. The fault core contains highly comminuted material that accommodates most of the cumulative shear strain while the damage zone consists of fragmented and brecciated rock with little or no shear displacement (Faulkner et al., 2003). Brittle deformation in the damage zone is generated by coseismic transient loading conditions; either by rapid reduction of normal stress (Brune et al., 1993), local strain near fracture tips (Reches and Dewers, 2005), and/or the propagation of shock waves during supershear rupturing (Doan and Gary, 2009). Coseismic fracturing and fragmentation, the extent and magnitude of which is controlled by the loading rate, may be an important component of the energy budget of rupture events (Barber and Griffith, 2017; Ghaffari et al., 2019; Rockwell et al., 2009; Wilson et al., 2005). The most extreme deformation caused by coseismic dynamic fracturing is thought to be expressed in so-called pulverised rocks, which have extremely high fracture densities and low shear strain. These rocks can be found tens to hundreds of meters from their fault core (Dor et al., 2006a; Fondriest et al., 2015; Mitchell et al., 2011; Rempe et al., 2013).

The close link between the variation of strength with strain rate and fragmentation behaviour has been demonstrated with a variety of dynamic uniaxial compression experiments (Barber and Griffith, 2017; Doan and Billi, 2011; Doan and Gary, 2009a; Ghaffari et al., 2019; Yao et al., 2020; Yuan et al., 2011a). Furthermore, fragmentation laws have been proposed that describe the variation of fragment size in an expanding shell as a function of the applied strain rate (Glenn and Chudnovsky, 1986; Grady, 1982; Levy and Molinari, 2010; Zhou et al., 2006a, 2006b); all of these models consistently predict that, at high strain rates, fragment size has an inverse power-law relationship with strain rate with an exponent of 2/3. This exponent arises as a consequence of the equilibrium conversion of kinetic energy released in fragmentation ($U_k \propto s^5 \dot{\varepsilon}^2$, where s is the fragment size) to fracture surface energy ($U_s \propto s^2$) (Grady, 1982). Direct comparisons between fragmentation models and the products of compressive failure are problematic because the fragmentation of an expanding shell is a tensile process. However, in general, experimental studies have shown that the fragmentation models overestimate average fragment sizes and/or do not follow a power law with the expected exponent (Ghaffari et al., 2019; Hogan et al., 2012, 2013; Lankford and Blanchard, 1991; Rae et al., 2020; Wang and Ramesh, 2004). Nevertheless, the combination of experimental and/or theoretical fragmentation models with field observations of naturally fragmented rock masses provides an important opportunity to determine transient loading conditions during coseismic deformation or other high-strain rate geoprocesses (Rowe and Griffith, 2015).

In this study, we aim to investigate the fragmentation behaviour of rocks under dynamic loading, characterising how fragment size and shape vary as functions of strain rate, therefore providing potential diagnostic indicators of transient loading conditions in naturally deformed rocks. To achieve this, we conducted quasi-static and dynamic uniaxial loading experiments on rock materials, determining dynamic rock mechanical properties and performing post-mortem analysis of the generated rock fragments. For this study, we decided to limit our investigation to sedimentary and metamorphic rocks: sandstone, quartzite, limestone, and marble. These rock types were chosen because, first, pulverisation has been widely reported in association with faults hosted in sandstones (Dor et al., 2006a, 2006b; Key and Schultz, 2011; Peppard et al., 2018) and carbonates (Agosta and Aydin, 2006; Fondriest et al., 2015; Sagy and Korngreen, 2012; Schröckenfuchs et al., 2015), and second, it allowed us to investigate the effect of porosity on fragmentation and dynamic material properties in lithologies with similar mineralogies.

2. Methods

2.1. Material description

The sandstone used in this study was quarried by TRACO Deutsche Travertin Werke GmbH at Seeberg near Gotha, Germany, hereafter termed 'Seeberger Sandstone'. Quartzite was acquired from Taunus-Quartzit-Werke GmbH & Co., Wehrheim, Germany, hereafter termed 'Taunus Quartzite'. Limestone was acquired from Savonnières-en-Perthois, Lorraine, France, hereafter termed 'Savonnières Limestone". Marble was acquired from the Amso International Company, Tuscany, Italy, hereafter termed 'Carrara Marble'.

The Seeberger Sandstone is composed of 89% quartz, ~10% phyllosilicates (mostly clay minerals and subordinate micas), and minor accessory minerals (Ebert et al., 2014). Grain sizes range between ~50–150 μm (Fig. 1). Macroscopically, weakly developed bedding and Liesegang banding can be observed, but do not cause significant mechanical anisotropy. The bulk density and porosity of the Seeberger Sandstone was determined by He-pycnometry to be 2130 ± 21 kg m^{-3} and 20.0 ± 0.8% respectively. The Taunus Quartzite is composed of 91% quartz, ~8% phyllosilicates, and minor accessory minerals (Ebert et al., 2014). Grain sizes range from ~100–400 μm (Fig. 1). The quartzite contains minor joints with an approximate spacing of 10 cm, the joints are commonly mineralized with chlorite. The bulk density and porosity of the Taunus Quartzite was determined by He-pycnometry to be 2645 ± 6 kg m^{-3} and 0.6 ± 0.1% respectively. The Savonnières Limestone is an oolitic grainstone with partial sparitic cement. Vacuolar ooids are common and the rock contains occasional shell fragments. Mineralogically, the rock is composed of close to 100% calcite. The ooids typically range in size from 400 to 750 μm (Fig. 1). The bulk density and porosity of the Savonnières Limestone was determined by He-pycnometry to be 1881 ± 31 kg m^{-3} and 31.4 ± 1.1% respectively. The Carrara Marble is composed of 98% calcite, and minor quantities of quartz, mica, dolomite, epidote, and pyrite (Pieri et al., 2001). Grain sizes range from 200 to 400 μm. Calcite grains are commonly twinned (Fig. 1). In hand specimen, the marble is massive and homogeneous. The bulk density and porosity of the Carrara Marble was determined by He-pycnometry to be 2711 ± 6 kg m^{-3} and 0.3 ± 0.0% respectively.

The samples used for rock deformation experiments were cored from blocks of each lithology (Fig. 1a). Typical samples were 39.0–41.0 mm in diameter, however cores of the Taunus Quartzite were ~ 35.0 mm in diameter for a number of reasons: firstly, the Taunus Quartzite is very strong, narrower diameter cores made it easier to achieve failure in split-Hopkinson pressure bar (SHPB) experiments. Secondly, the joints within the Taunus Quartzite made drilling challenging, reducing core diameter made it easier to produce appropriate samples. Additionally, cores of the Savonnières Limestone were ~ 54 mm in diameter for quasi-static uniaxial compressive strength (UCS) testing due to the material's extreme weakness; larger diameter samples ensured that a larger force could be applied to the samples and that a greater amount of data could be recorded in the elastic regime. The lengths of the samples were maintained such that samples had 2:1 aspect ratios (length-to-diameter ratio) for quasi-static UCS testing (Hawkes and Mellor, 1970; Hawkins, 1998) and had ~1:1 aspect ratios for SHPB experiments (Zhang and Zhao, 2014; Zhou et al., 2011). After drilling, all samples were ground to produce plane-parallel faces and then dried in an oven at 50 °C for 48 h. In total, 90 experiments were conducted in this study. 27 and 20 experiments were carried out on the Seeberger Sandstone and Taunus Quartzite, respectively. 18 and 25 experiments were carried out on the

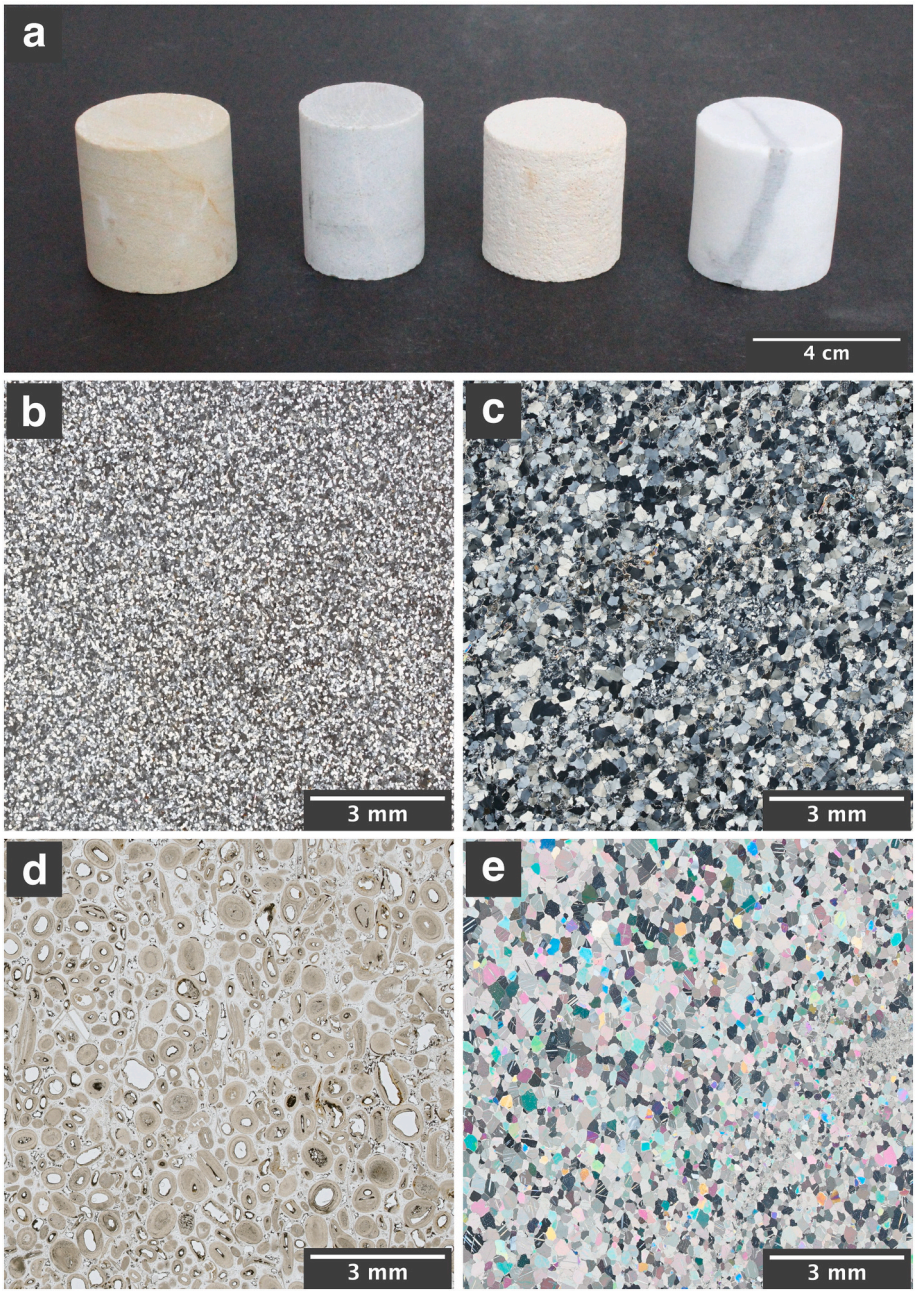

Fig. 1. Sample lithologies. a) Hand specimens of (from left to right) Seeberger Sandstone, Taunus Quartzite, Savonnières Limestone, and Carrara Marble. b-e) Thin section images of the four lithologies: b) Seeberger Sandstone under cross-polarised light, c) Taunus Quartzite under cross-polarised light, d) Savonnières Limestone under plane-polarised light, and e) Carrara Marble under cross-polarised light.

Savonnières Limestone and Carrara Marble, respectively. Sample dimensions for each experiment are listed in the Supplementary Online Material.

2.2. Experimental rock deformation

2.2.1. Quasi-static testing

Uniaxial compression experiments under quasi-static conditions were performed with a servo-controlled Form+Test Alpha 2–3000 S hydraulic press in the Department of Geology at the University of Freiburg. Displacement gauges were used to measure the longitudinal and transverse strains in the samples. From these strains, the elastic (Young's) modulus and Poisson's ratio of the samples were determined. Experiments were run under constant loading-rate conditions, which, within the elastic loading regime leads to constant strain rates. Experiments were conducted at strain rates between 5.3×10^{-6} and 3.4×10^{-5} s^{-1}. Between 3 and 8 quasi-static experiments were carried out for each lithology.

2.2.2. Dynamic testing

Uniaxial compression experiments under dynamic conditions were performed with a split Hopkinson pressure bar (SHPB) in the Department of Geology at the University of Freiburg. SHPBs are comprised of three bars: striker, incident, and transmission. The sample is positioned between and in contact with the incident and transmission bars. The striker bar is accelerated towards the front-end of the incident bar, generating a stress wave that propagates towards the sample and transmission bar. The amplitude of the stress wave is low enough not to

induce permanent deformation in the bars but can be high enough to induce failure in the sample material. Strain gauges are attached to the incident and transmission bars such that the stress and strain history of the sample can be determined (see Supplementary Material). Here, we determine the strain rate for a given experiment by taking the average strain rate during loading with one standard deviation errors (see Supplementary Material). Strain rates in failed specimens during SHPB experiments were between 35.5 ± 7.4 and 345.5 ± 83.2 s^{-1}. A detailed description of the methodology and processing of SHPB data, including strain rate and strength determination, is provided in the Supplementary Material and provided in a GitHub Repository. General descriptions of the methodology of SHPBs can be found by Aben et al. (2017); Chen and Song (2010); Xia and Yao (2015); Zhang and Zhao (2014); Zhou et al. (2011); and Zwiessler et al. (2017). Samples were recovered from the SHPB by collection in a secure box lined with a polyethylene bag.

2.3. Fragment analysis

2.3.1. Size

On average, we were able to recover 88.2% of the mass of each sample from the SHPB experiments, recovery was generally poorer in the sandstone and limestone, with average recoveries of 83.4% and 84.4% respectively, while 95.5% and 88.6% recoveries were achieved with the quartzite and marble respectively (see GitHub repository for further details). Fragment size distributions were obtained by sieving the fragmented rock masses resulting from the experiments. Each sample of the same lithology were passed through identical sieve stacks, although sieve stacks were varied between lithology. Each sieve stack had at least 7 sieves ranging from 16 mm to 0.125 mm square apertures. Sieving was carried out dry and shaking was carried out by hand for a duration of one minute per sample.

A consequence of using sieving to determine fragment size distributions is that it results in mass-size distributions, as opposed to number-size distributions. A variety of statistical distributions can be used to fit fragment size distributions from failure events (see Grady, 2010). Here, we have chosen to use cumulative Weibull distributions:

$$\frac{M(s)}{M_T} = 1 - e^{-(s/\lambda)^k} \tag{2}$$

where $M(s)$ is the cumulative mass of fragments that have a size less than s; M_T is the total sample mass; and λ and k are the Weibull distribution parameters. There is no theoretical basis for our usage of the Weibull distribution which we chose only for its simplicity, general usage (Grady, 2009), and similarity to the shape of our data. We note that other distributions could have been used to fit our fragment size data, e.g., Rayleigh (Levy and Molinari, 2010), log-normal (Wang and Ramesh, 2004), or generalized extreme value (Hogan et al., 2012). Non-linear least squares fitting was used to determine the Weibull distribution parameters. The median of a Weibull distribution, $\bar{s}$, can be calculated as:

$$\bar{s} = \lambda\, ln(2)^{1/k} \tag{3}$$

In the case of the quartzite, limestone, and marble samples, no more than 26% and on average 2%, 8%, and 16% respectively of the total mass of the samples passed the finest sieve. Thus, for these lithologies, the median fragment size is an interpolated value within the distribution. However, the sandstone produced substantially finer fragments such that on average 42% of the total mass of the samples passed the finest sieve. In 5 sandstone samples, the mass percentage passing through the finest sieve exceeded 50%, and therefore the calculated median fragment size is extrapolated below the size of the finest sieve size. We were unable to extend these distributions to finer fragment sizes due to unreliability of dry sieving through finer sieves. Additionally, we attempted to use laser diffraction granulometry (Malvern MasterSizer 3000) on the fine fragments but were unable to achieve consistent overlap between sieving and laser diffraction analyses and between different runs of the laser diffraction granulometer on the same sample to extend the fragment size distributions to smaller fragment size. Our problems of integrating fragment size distributions across different methodologies are similar to those reported by Rockwell et al. (2009) on pulverised rocks from the San Andreas and Garlock faults in southern California.

2.3.2. Shape

The shapes of fragments generated by the experiments were determined by image analysis. We focussed on two size fractions: fragments larger than 2 mm, and fragments from 0.5 to 2 mm in size. These size fractions had to be imaged separately and followed different image processing procedures for a variety of practical reasons (for details, see Supplementary Material). For the fragments larger than 2 mm, all fragments in the sample were analysed. The total number of fragments in each of these distributions ranged from 122 to 629, depending on sample. For the fragments between 0.5 and 2 mm, subsampling was required and four images, each of different subsamples, were acquired. After ensuring consistency between the distributions of each subsample, the fragment shape data from all four images were combined into a single distribution. The total number of fragments in each of these distributions ranged from 1980 to 6660, depending on sample (for details, see Supplementary Material and Supplementary Online Material). Images were processed using the Fiji software package (Schindelin et al., 2012; see Supplementary Material) and fragment shape parameters were determined for each fragment. Here, we have considered two shape factors, circularity, C, and axial ratio, AR (Heilbronner and Barrett, 2014):

$$C = 4\pi \frac{A}{P^2} \tag{4}$$

$$AR = \frac{w}{l} \tag{5}$$

where A is the area of the fragment, P is the perimeter of the fragment, w is the minor axis length of the best-fitting ellipse, and l is the major axis length of the best-fitting ellipse. C has a value of 1 for a perfect circle and approaches 0 as the shape's perimeter increases relative to its area. AR has a value of 1 for a perfectly equant shape, i.e. any regular polyhedra, and approaches 0 as the shape becomes increasingly elongate.

3. Results

3.1. Mechanical data

In general, results of mechanical testing demonstrate dynamic strength increase under uniaxial compression at large strain rates. The quasi-static and dynamic uniaxial compressive strength (UCS) values can be individually fitted to the scaling relationship of Kimberley et al. (2013) (Eq. 1) by non-linear least squares fitting (Fig. 2). The characteristic stress (i.e. the UCS) of the sandstone, quartzite, limestone, and marble were determined to be 55.8 ± 3.6, 243.3 ± 15.6, 18.6 ± 1.5, and 97.8 ± 6.7 MPa respectively (Table 1). The characteristic strain rates of the sandstone, quartzite, limestone, and marble are 322 ± 92, 280 ± 92, 241 ± 78, and 144 ± 33 s^{-1}, respectively (Table 1).

3.2. Fragment size distributions

Fragment size distributions and their fitted Weibull distributions for the sandstone, quartzite, limestone, and marble are shown on Fig. 3a-d. All distributions are characterised by increasing fractions of fine-grained material at larger strain rates. Weibull distributions produce very good fits to the fragment size distributions of the Savonnières Limestone, while providing good fits to the Seeberger Sandstone and Taunus Quartzite distributions. The Carrara Marble distributions are, in general,

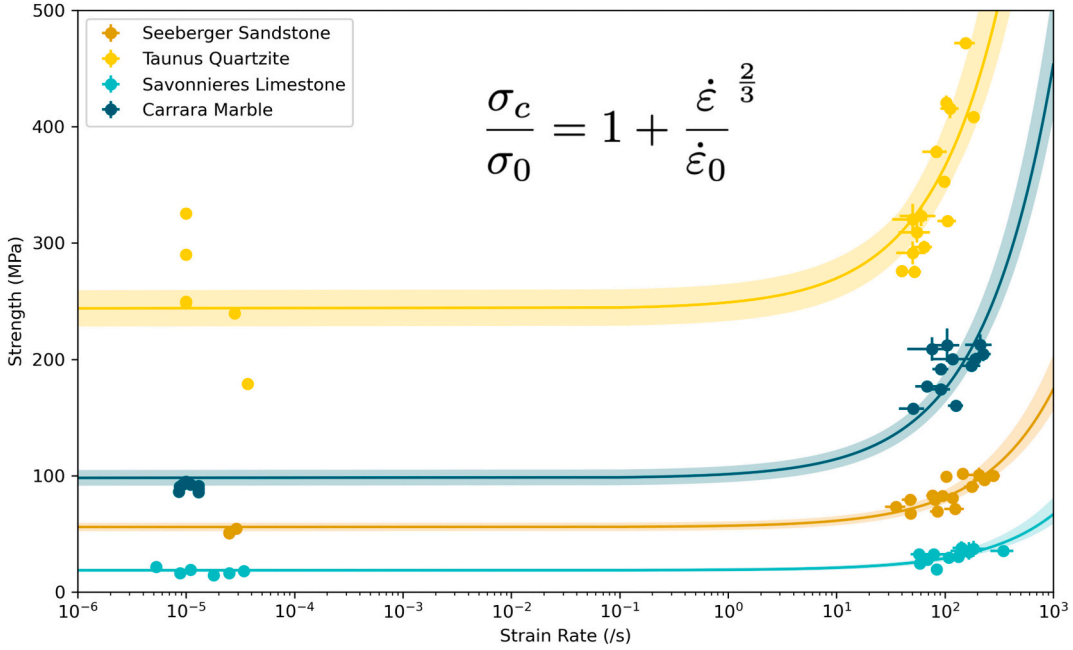

Fig. 2. Compressive strength data from quasi-static and dynamic testing at various strain rates. In general, scatter as a result of differences between samples is most pronounced in the high rate experiments that have considerably larger uncertainties (see Supplementary Material for details). The exception to this occurs with the Taunus Quartzite samples where considerable variability in the quasi-static strength is observed, which we attribute to the sporadic occurrence of joints in the lithology. Each lithology follows the universal scaling relationship of Kimberley et al. (2013), each fitted curve is shown with 1 σ error envelopes. Data presented with a linear x-axis are shown in Supplementary Fig. 2. The material parameters, σ_0 and $\dot{\varepsilon}_0$, and their uncertainties are reported in Table 1.

Table 1
Measured material properties of the Seeberger Sandstone, Taunus Quartzite, Savonnières Limestone, and Carrara Marble.

	Seeberger Sandstone	Taunus Quartzite	Savonnières Limestone	Carrara Marble
ρ (kg m^{-3})	2130 ± 21	2645 ± 6	1881 ± 31	2711 ± 6
φ (%)	20.0 ± 0.8	0.6 ± 0.1	31.4 ± 1.1	0.3 ± 0.0
E (GPa)	13.8 ± 0.6	38.1 ± 5.9	11.5 ± 2.1	44.8 ± 3.0
ν	0.373 ± 0.050	0.099 ± 0.022	0.197 ± 0.044	0.245 ± 0.026
σ_0 (MPa)	55.8 ± 3.6	243.3 ± 15.6	18.6 ± 1.5	97.8 ± 6.7
$\dot{\varepsilon}_0$ (s^{-1})	322 ± 92	280 ± 92	241 ± 78	144 ± 33
N	2.90 ± 0.63	1.45 ± 0.36	0.65 ± 0.23	1.45 ± 0.41
V_p (m s^{-1}) *	3413 ± 480	3837 ± 298	2602 ± 273	4433 ± 181

E = Quasi-static Elastic Modulus, ν = Quasi-static Poisson's Ratio, ρ = Bulk Density, φ = Porosity, σ_0 = Characteristic Stress (i.e. Quasi-static Uniaxial Compressive Strength), $\dot{\varepsilon}_0$ = Characteristic Strain Rate, N = Power-law exponent of fragment size vs. strain rate, V_p = P-wave velocity. * Calculated from elastic properties, $v_p = \sqrt{\frac{E(1-\nu)}{(1+\nu)(1-2\nu)\rho}}$.

less well fitted by Weibull distributions, however, the median values of those fitted distributions tend to closely match the linearly interpolated 50th percentile value of the distribution and therefore, we continued to use the Weibull distribution fits to determine the average grain size of each distribution. Average fragment sizes for each lithology decrease with increasing strain rate (Fig. 4). Each lithology follows an inverse power law where the exponents for the sandstone, quartzite, limestone, and marble are 2.90 ± 0.63, 1.45 ± 0.36, 0.65 ± 0.23, and 1.45 ± 0.41, respectively.

3.3. Fragment shape distributions

Overall, the shape distributions of fragments do not vary as functions of strain rate or with lithology (Figs. 5 and 6). For the fragments larger than 2 mm and across all lithologies, the average circularity is 0.733 ± 0.087 and the average axial ratio is 0.627 ± 0.146 (Table 2). No individual distribution, regardless of strain rate or lithology, is an outlier of these average values. For the fragments that range between 0.5 and 2 mm and across all lithologies, the average circularity is 0.598 ± 0.180 and the average axial ratio is 0.642 ± 0.152 (Table 2). The average circularity of these smaller fragments is less than the average circularity of the larger fragments while axial ratios remain similar, additionally the standard deviations of the distributions of these finer fragments is generally larger. We largely attribute these variations to differences in method between larger and smaller fragments (see Supplementary Material). However, we observe similar trends in the fragment shape distributions from sample to sample between the different fragment size fractions (Figs. 5 and 6), demonstrating the overall robustness of the fragment shape analysis.

4. Discussion

4.1. Mechanical properties

4.1.1. Strength

The quasi-static strengths of the Seeberger Sandstone, Taunus Quartzite, Savonnières Limestone, and Carrara Marble determined in this study are generally consistent with previous measurements of the same lithologies (Table 3). The only study of the same lithologies where measured strength values differ by more than 2σ uncertainties is that of Millon et al. (2016); we note that Millon et al. used larger samples with greater aspect ratios (3:1) than our samples, which may be responsible for lower values of UCS (Hawkes and Mellor, 1970; Hawkins, 1998).

4.1.2. Characteristic strain rate

Characteristic strain rates for rate dependency, whether defined strictly according to the scaling relationship of Kimberley et al. (2013) or more generally as the strain rate for the transition between quasi-static and dynamic deformation, are less widely reported than strength values. Dynamic strength data for the Seeberger Sandstone has been reported by

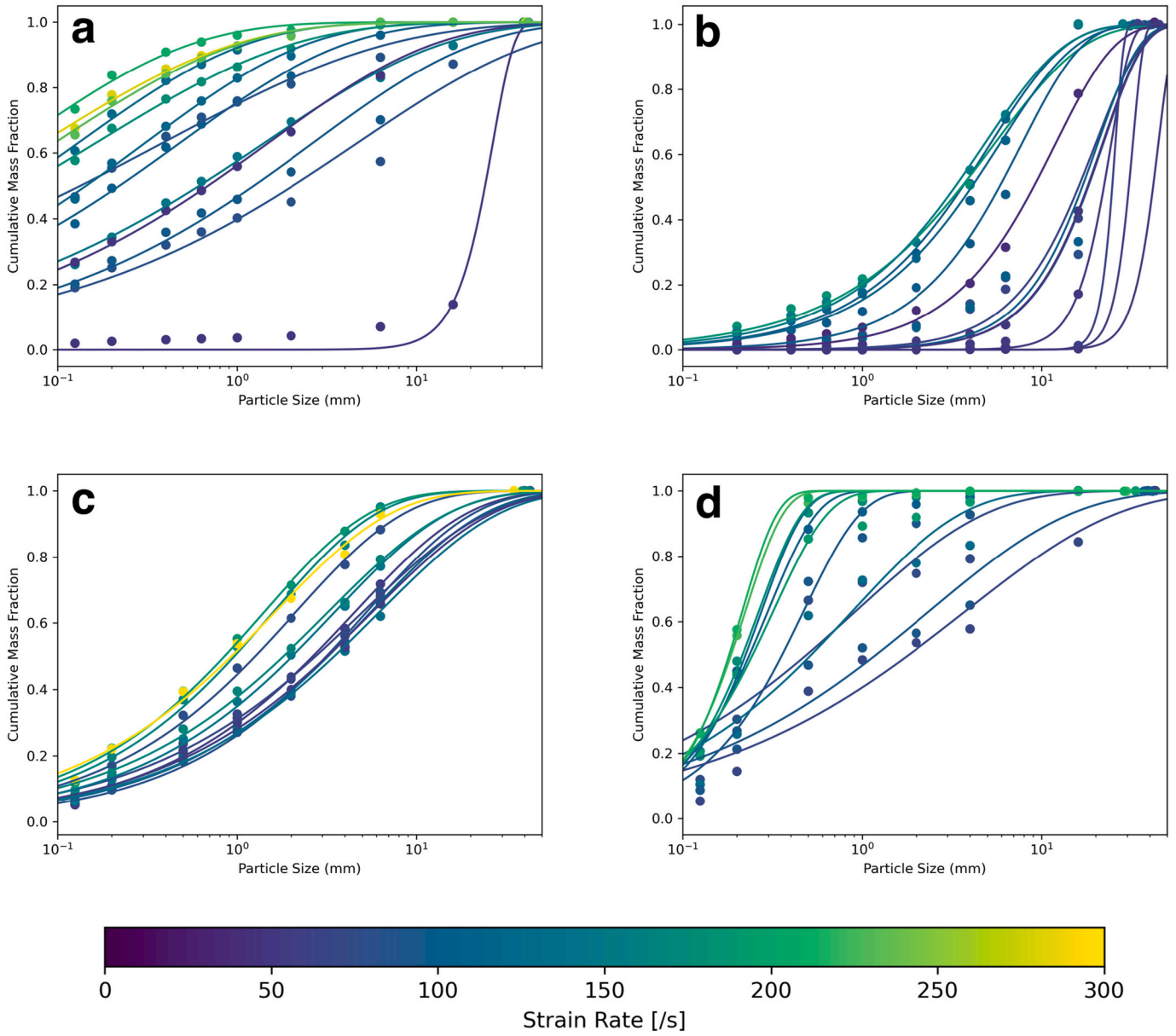

Fig. 3. Cumulative mass fragment size distributions coloured by strain rate for a) Seeberger Sandstone, b) Taunus Quartzite, c) Savonnières Limestone, and d) Carrara Marble.

Millon et al. (2016) and Zwiessler et al. (2017). Millon et al. (2016) did not directly report a characteristic rate but instead demonstrated dynamic increase factors (DIFs) between 3.6 and 5.3 at strain rates between 275 and 350 s^{-1}; ultimately suggesting a characteristic strain rate (where at that rate, DIF is 2) that is less than 275 s^{-1} but greater than $\sim 10^{1}$ s^{-1}. Zwiessler et al. (2017), on the other hand state the characteristic rate of the Seeberger Sandstone to be 170 s^{-1}. Both of these studies appear to demonstrate lower values of characteristic strain rate than reported here, however we note that our results are based on a considerably larger data set and that our results provide quantified, and quite large, statistical uncertainties. To our knowledge, dynamic strength properties of the Taunus Quartzite have never been reported. Millon et al. (2016) also investigated the dynamic strength of the Savonnières Limestone. They found DIFs of 4.3–4.9 over strain rates from 345 to 515 s^{-1}; suggesting a characteristic strain rate less than 345 but greater than $\sim 10^{1}$ s^{-1}. Again, this is lower than the value of the characteristic rate reported in this study, however again, our study is based on a larger data set, and provides more constraint on the value of the characteristic strain rate. Furthermore, we note that our study is consistent with the results of Millon et al. (2016) in that the characteristic rates of both the Seeberger Sandstone and Savonnières Limestone are similar, being within uncertainties of each other. Finally, the characteristic strain rate of the Carrara Marble has been reported by Zwiessler et al. (2017) as 65 s^{-1}. Additionally, Zou and Wong (2016) reported DIFs between 4.0 and 7.0 at strain rates between 100 and 600 s^{-1}, suggesting a characteristic strain rate between 10 and 100 s^{-1}. Our value for the characteristic strain rate of the Carrara Marble is greater than both Zwiessler et al. (2017) and Zou and Wong (2016) suggest, however, our results are consistent with the results of Zwiessler et al. (2017) in that the characteristic rate of the Carrara Marble is significantly less than the characteristic rate of the Seeberger Sandstone. Additionally, in a study on the dynamic deformation of the Carrara Marble, Doan and Billi (2011) found a transition from splitting to pulverisation at peak strain rates of ~100 s^{-1}. However, their results show a curious lack of systematic increase in strength between peak rates of ~50–250 s^{-1}.

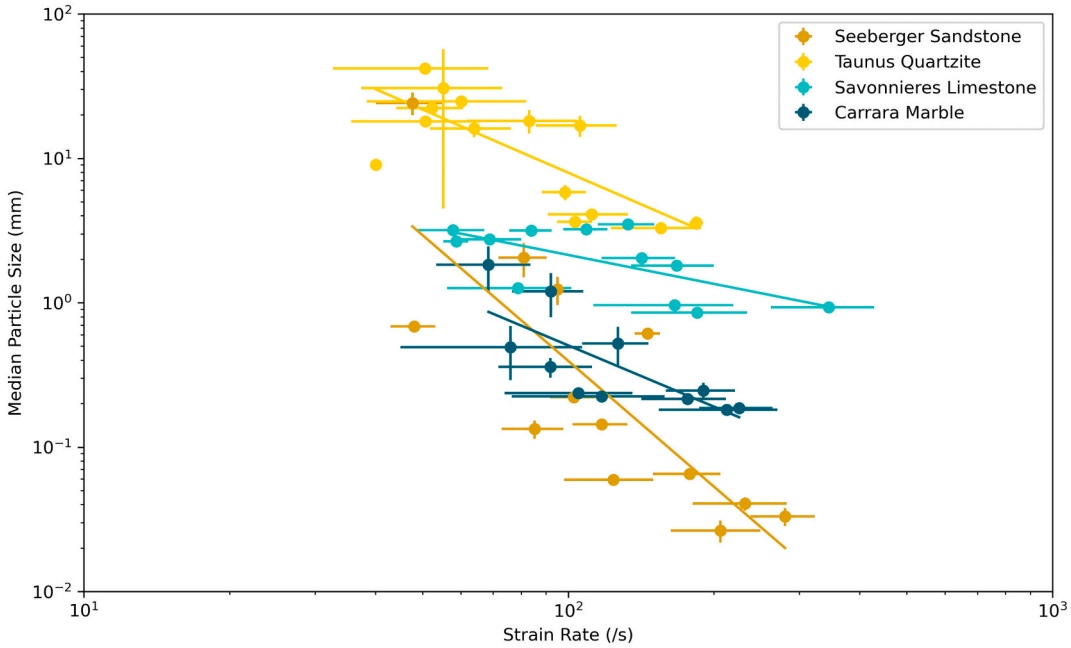

Fig. 4. Median fragment size variation with strain rate. Error bars parallel to the x-axis (x-error bars) are the 1σ uncertainty of the experimentally determined strain rate, y-error bars are the 1σ propagated uncertainty from the uncertainties of the fitted parameters of the Weibull fragment size distributions. x- and y- error bars are shown for all points where the error bars are larger than the size of the point.

Other studies of dynamic strength in sedimentary and metamorphic rocks are generally consistent with the results of our study. Green et al. (1972) conducted one of the earliest studies on the dynamic strength properties of rocks and found a transition to dynamic behaviour in Solnhofen Limestone at ~10^2 s^{-1}. Howe et al. (1974) found dynamic strength increases in the anisotropic Yule Marble at rates >10 s^{-1}. In a study on the Berea Sandstone and Indiana Limestone, Blanton (1981) demonstrated a lack of dynamic strength effects at strain rates up to 10 s^{-1}. On the same limestone, Frew et al. (2001) found DIFs of up to 1.7 at rates of ~100 s^{-1}. Rosakis (1999) reported dynamic strength properties of Dionysus-Pentalicon Marble (see Bhat et al., 2012), demonstrating DIFs of 2 at ~400 s^{-1}. In sandstones, Alam et al. (2015) found DIFs up to ~1.8 at strain rates up to ~1 s^{-1} in an investigation of the Kota Sandstone while Liu et al. (2012) conducted experiments on Qinling Sandstone at rates between 50 and 100 s^{-1} and found DIFs between 1.6 and 3.2, suggesting a characteristic strain rate of ~60 s^{-1}. Most recently, Fondriest et al. (2017) investigated the Mendola Dolostone and found the onset of pulverisation at rates of ~120 s^{-1}, albeit with limited dynamic strength increase between 40 and 300 s^{-1}.

Our results show that the characteristic strain rates of the Seeberger Sandstone, Taunus Quartzite, and Savonnières Limestone, with values of 322 ± 92, 280 ± 92, and 241 ± 78 s^{-1} respectively, are all within uncertainty of each other (Table 1). In a previous study, we reported the characteristic strain rates of felsic crystalline rocks; a granite and a transversely isotropic gneiss (Rae et al., 2020), to be within uncertainty of each other (and independent of anisotropy) with an average value of 229 ± 81 s^{-1}, remarkably similar to the characteristic rates of the Seeberger Sandstone, Taunus Quartzite, and Savonnières Limestone. This suggests that lithological variability of characteristic strain rate is minor or even negligible for rocky materials, particularly given the large uncertainties that arise as a result of inter-sample variability, in addition to the challenges of defining a precise and accurate representative strain rate for SHPB, and other dynamic mechanical testing, techniques (Aben et al., 2017; Ramesh et al., 2015; Supplementary Material).

The Carrara Marble, with a characteristic rate of 144 ± 33, is the only lithology we have investigated to have a significantly different value of characteristic strain rate. By the consideration of characteristic length and time scales, Kimberley et al. (2013) suggested that the characteristic strain rate in their scaling relationship can be related to mechanical and microstructural properties of the material:

$$\dot{\varepsilon}_0 \propto \frac{v_p}{\bar{s}} \frac{K_{IC}}{E} \eta^{\nu_4} \tag{6}$$

where v_p is the p-wave speed, $\bar{s}$ is the average flaw size, K_{IC} is the mode-I fracture toughness, E is the elastic modulus, and η is the flaw density. By this consideration, the Carrara Marble must either possess comparatively low values of v_p, K_{IC}, or η, or large values of $\bar{s}$ or E. Based on the elastic properties determined in this study, the wave speed of the Carrara Marble is significantly greater than that of the other lithologies; while the elastic modulus, though large, is comparatively similar to the other non-porous lithology, i.e., the Taunus Quartzite. The mode-I fracture toughness of the Carrara Marble has been measured by Atkinson (1979) and Meredith et al. (1984) as 0.64 and 0.87 MPa $m^{1/2}$, respectively. Mode-I fracture toughnesses for the other lithologies in this study have not been determined, however in comparison to literature values for sandstones, quartzites, and limestones generally (**Table 4**), the fracture toughness of the Carrara Marble is low, though not by a large enough factor to fully account for the reduced characteristic strain rate. The microstructural properties of flaw size and flaw density are extremely challenging to measure within a real rock (Housen and Holsapple, 1999), and therefore, it may be the case that the Carrara Marble simply has an unusual distribution of flaws to explain the discrepancy in characteristic strain rate. Nevertheless, the scaling relationship of Kimberley et al. (2013) assumes that the mode-I fracture toughness is a constant value; but fracture toughness is known to increase as a function of strain rate (Bhat et al., 2012; Ravi-Chandar and Knauss, 1984a; Zhang and Zhao, 2014). Consequently, the behaviour of the Carrara Marble may be a consequence of a decreased sensitivity of fracture toughness with strain rate in comparison to other rocks.

4.2. *Fragment characteristics*

4.2.1. *Fragment size – an empirical compressive fragmentation relationship*

Our results demonstrate the general relationship that increasing

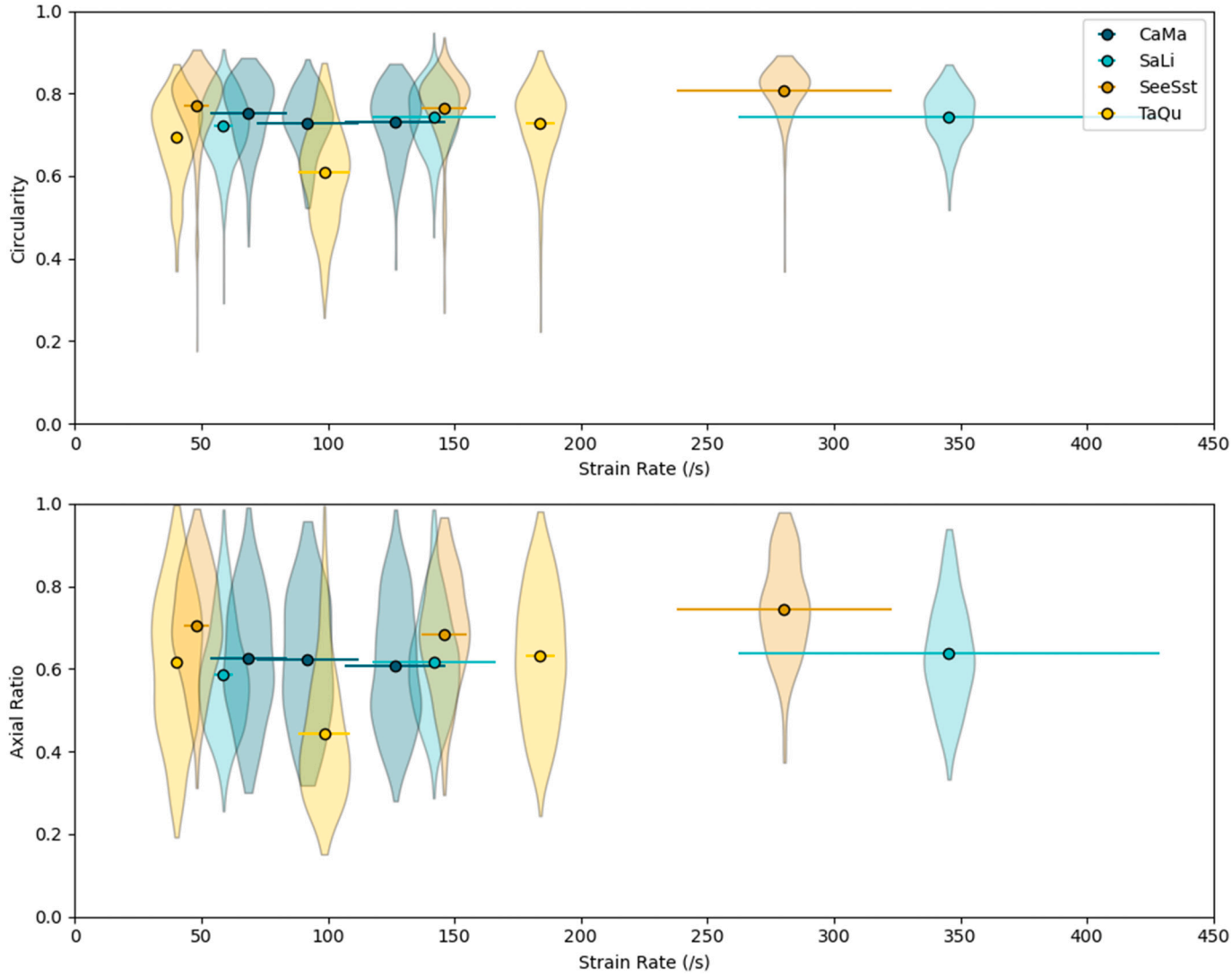

Fig. 5. Fragment shape distributions for all fragments >2 mm as a function of strain rate. Distributions of fragment shape (circularity and axial ratio) for each sample are shown as kernel density estimates. Each point shows the mean shape parameter plotted against the strain rate, where the x-error bar shows the uncertainty in the strain rate (see Supplementary Material for details).

strain rate results in finer fragmentation under uniaxial compression. This observation is in agreement with a large number of previous studies (e.g., Barber and Griffith, 2017; Doan and Billi, 2011; Doan and d'Hour, 2012; Doan and Gary, 2009; Fondriest et al., 2017; Ghaffari et al., 2019; Hogan et al., 2012, 2016; Li et al., 2018; Millon et al., 2016; Rae et al., 2020; Yao et al., 2020; Yuan et al., 2011). Specific comparison of our fragmentation results with many of these studies is challenging for a variety of reasons. Firstly, fragment size distributions can be characterised by either mass or by number, converting number-size to mass-size distributions and vice versa is non-trivial. Secondly, even with the same type of distribution, its shape will depend on the method used to obtain that distribution (e.g., sieving, sedimentation, laser diffraction). Finally, there is no single common method of determining the "characteristic" size of a fragment size distribution. We arbitrarily chose to use the median of the fragment mass-size distribution (also known as D50) as the "characteristic" size of each distribution.

Despite these complexities, we find that the fragmentation behaviour of the Taunus Quartzite is very similar to the behaviour of felsic crystalline rocks (Rae et al., 2020), producing average fragment sizes of 40–1 mm at strain rates of 30–300 s^{-1} (Fig. 4). Somewhat expectedly, the Seeberger Sandstone produces considerably finer fragments at equivalent strain rates, which we attribute to the relative ease of fracturing and separating grains in a porous material. By comparison, the Savonnières Limestone produces coarser fragments than the Seeberger Sandstone but finer fragments than the Taunus Quartzite and other non-porous crystalline rocks (Fig. 4). We suggest that this may be a consequence of the relative grain sizes of the lithologies; the texture of the Savonnières Limestone is dominated by 0.5–1 mm diameter ooids, while the Seeberger Sandstone has an average grain size of ~0.1 mm. Our results on the fragmentation of Seeberger Sandstone and Savonnières Limestone can be compared to the results of Millon et al. (2016) who report fragment size distributions with D50 values from 19.9–1.6 mm at strain rates between 20 and 345 s^{-1} respectively for the Seeberger Sandstone, and D50 values between 21.4 and 0.46 mm at strain rates between 20 and 515 s^{-1} respectively for the Savonnières Limestone. These fragment sizes are generally consistent with the results of our study except for the average fragment size of the Seeberger Sandstone at large strain rates where we produced considerably finer fragments. In a study of the dynamic failure properties of the Carrara Marble, Doan and Billi (2011) found that pulverisation of marble was "easier" than pulverisation in granite. Our study is consistent with this observation, where, at the same strain rate, the Carrara Marble produces fragments at

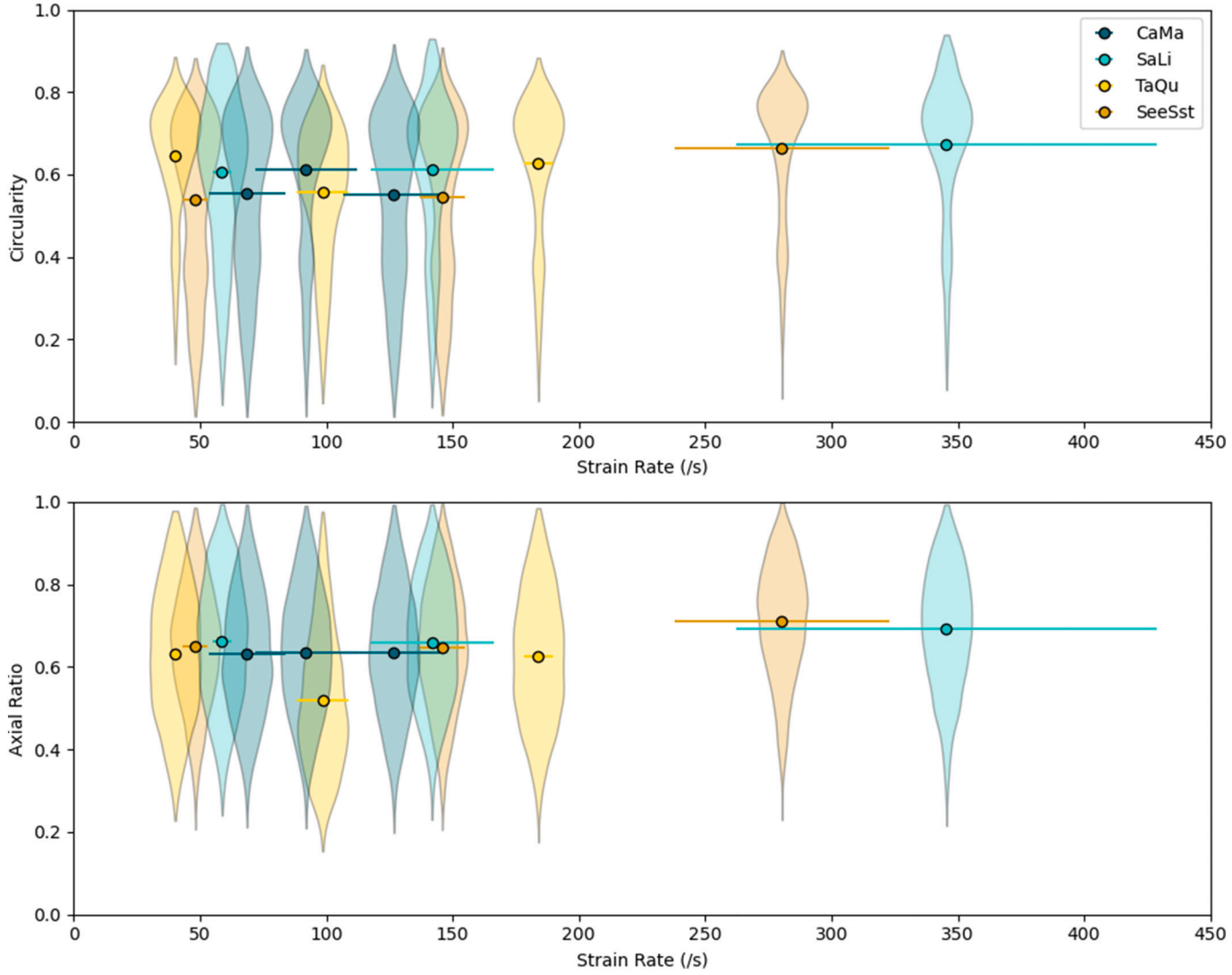

Fig. 6. Fragment shape distributions for all fragments $0.5 < x < 2$ mm as a function of strain rate. Distributions of fragment shape (circularity and axial ratio) for each sample are shown as kernel density estimates. Each point shows the mean shape parameter plotted against the strain rate, where the x-error bar shows the uncertainty in the strain rate (see Supplementary Material for details).

least one order of magnitude finer than the fragmentation of felsic crystalline rocks reported by Rae et al. (2020) and the quartzite of this study. The Carrara Marble even produces finer fragments than the Savonnières Limestone, which may be a consequence of its finer grain size.

A number of models have been proposed to determine average fragment size as a function of strain rate (Glenn and Chudnovsky, 1986; Grady, 1982; Levy and Molinari, 2010; Zhou et al., 2006a, 2006b). These models are principally concerned with tensile fragmentation of an expanding shell. While each model has important differences, all models predict that in the dynamic regime, fragment size is an inverse power law function of strain rate with an exponent of 2/3, a value that arises as a consequence of the assumption of equilibrium conversion of the kinetic energy released in fragmentation to fracture surface energy (Grady, 1982). The energy-based fragmentation models of Grady (1982) and Glenn and Chudnovsky (1986) do not explicitly address the issue of the statistical distribution of fragment sizes (Grady, 2007), while more recent dynamic models (Levy and Molinari, 2010; Zhou et al., 2006a, 2006b) have used the average of number-size distributions. Deviations from an exponent of 2/3 may reflect either additional energy sources, such as elastic strain energy (e.g. Glenn and Chudnovsky, 1986), or additional energy sinks, such as frictional heating, remnant kinetic energy, or plastic work. All of the rocks in this study demonstrate an inverse power law relation between median fragment size (determined from mass-size distributions) under uniaxial compressive failure and strain rate (Fig. 4). The exponents of those power-laws vary, depending on lithology, between 0.65 +/− 0.23 and 2.90 +/− 0.63 (Table 1). A direct comparison between these exponents and the exponents of the fragmentation models is challenging due to the complexity of converting mass-size and number-size distributions. Ghaffari et al. (2019) also reported an inverse power-law relationship between fragment size (from number-size distributions) and strain rate in uniaxial compression in Westerly Granite, however their exponent of 0.42 is considerably lower than a value of 2/3, unlike our results which produced exponents that were generally greater.

Tensile failure, as modelled in the expanding shell problem, is fundamentally different from compressive failure (Jaeger et al., 2007). The creation, activation, and growth of internal defects that occurs during compressive failure can make a material quite different from its pristine condition (Hogan et al., 2016), and large amounts of strain energy can be stored in brittle materials in compression which, when released, can generate very fine fragments (Ramesh et al., 2015).

Table 2
Summary of fragment shape distributions of Seeberger Sandstone, Taunus Quartzite, Savonnières Limestone, and Carrara Marble organised by fragment size fraction.

	Sample Size	Circularity		Axial Ratio	
Seeberger Sandstone	*n range*[1]	*μ range*[1]	*Mean σ*[1]	*μ range*[1]	*Mean σ*[1]
s > 2 mm	122–408	0.765–0.805	0.086	0.685–0.741	0.131
0.5 < s < 2 mm	5370–6660	0.544–0.664	0.189	0.649–0.712	0.145
Taunus Quartzite	*n range*[1]	*μ range*[1]	*Mean σ*[1]	*μ range*[1]	*Mean σ*[1]
s > 2 mm	352–499	0.610–0.729	0.106	0.444–0.631	0.166
0.5 < s < 2 mm	1980–3668	0.556–0.646	0.157	0.521–0.633	0.161
Savonnières Limestone	*n range*[1]	*μ range*[1]	*Mean σ*[1]	*μ range*[1]	*Mean σ*[1]
s > 2 mm	431–629	0.720–0.743	0.074	0.586–0.638	0.131
0.5 < s < 2 mm	3742–4215	0.605–0.672	0.180	0.659–0.692	0.150
Carrara Marble	*n range*[1]	*μ range*[1]	*Mean σ*[1]	*μ range*[1]	*Mean σ*[1]
s > 2 mm	137–272	0.727–0.753	0.082	0.608–0.626	0.155
0.5 < s < 2 mm	5370–6531	0.550–0.612	0.194	0.633–0.636	0.151
Average	*n*	*Mean μ*[2]	*Mean σ*[2]	*Mean μ*[2]	*Mean σ*[2]
s > 2 mm	4426	0.733	0.087	0.627	0.146
0.5 < s < 2 mm	55,625	0.598	0.180	0.642	0.152

n = sample size
μ = mean value of a fragment size distribution
σ = standard deviation of a fragment size distribution.
[1] derived from all 3 distributions for each lithology
[2] derived from all 12 distributions

Table 3
Comparison of uniaxial compressive strengths of the lithologies in this study with literature values.

	Seeberger Sandstone	Taunus Quartzite	Savonnières Limestone	Carrara Marble
This study	55.8 ± 3.6	243.3 ± 15.6	18.6 ± 1.5	97.8 ± 6.7
(Poelchau et al., 2014)	67.3 ± 2.7	292 ± 39	–	–
(Millon et al., 2016)	42.3 ± 2.4	–	9.8 ± 1.5	–
(Zwiessler et al., 2017)	60.4 ± 4.6	–	–	88.8 ± 5.7
(Van Stappen et al., 2019)	–	–	14.5 ± 1.7 (large) 15.7 ± 3.5 (small)	–
(Doan and Billi, 2011)	–	–	–	~100
(Fredrich et al., 1989)	–	–	–	100*

* 5 MPa confining stress

Consequently, compressive fragmentation cannot be directly compared to tensile fragmentation models. Hogan et al. (2016) and Ramesh et al. (2015) have developed a method to convert compressive strain rates to equivalent tensile strain rates such that compressive failure could be compared to tensile fragmentation models. In a previous study (Rae et al., 2020), we found that applying this conversion method caused the fragment relationships of multiple lithologies to collapse onto a single power-law relationship, however, the exponent of that relationship remained significantly different from the expected exponent of 2/3. The results presented here could be analysed with the same method to produce a similar result; however, we have decided to take a more phenomenological approach and derive a simple empirical relationship between strain rate and fragment size. To achieve this, we first normalise the compressive strain rate by the characteristic strain rate for each lithology. Then we attempted to find a normalisation factor for the average fragment size that caused the results to collapse onto a single power law. Noting that the method of Hogan et al. (2016) and Ramesh et al. (2015) achieved the collapse of the data to a single power-law, we decided to attempt a normalisation factor akin to the characteristic length used in their method. That characteristic length, s_0, is determined by considering the characteristic time, t_0, for the growth of a cohesive crack under external loading and the sound velocity of the material (Camacho and Ortiz, 1996; Drugan, 2001):

$$s_0 = v_p\, t_0 = \frac{K_{IC}{}^2}{2\sigma_t{}^2} \tag{7}$$

where σ_t is the tensile strength of the material. Noting that the tensile strength of rocks is typically some constant fraction of the compressive strength (e.g., Hogan et al., 2016), we reduce the characteristic length scale to remove the constant terms, i.e.:

$$s_0 = \frac{K_{IC}{}^2}{\sigma_0{}^2} \tag{8}$$

While K_{IC} values for the Carrara Marble have been determined experimentally (Atkinson, 1979; Meredith et al., 1984), K_{IC} is unknown for the other lithologies. Instead, we take the average value of K_{IC} from similar lithologies and include the effect of considerably larger uncertainties (Table 4).

Normalisation of the strain rates and fragment sizes for all the experiments in this study and the experimental results of Rae et al. (2020) are shown on Fig. 7. We notice that this normalisation results in the collapse of all non-porous lithologies to a single inverse power-law relation, and the porous lithologies (Seeberger Sandstone, φ = 20.0 ± 0.8%; Savonnières Limestone, φ = 31.4 ± 1.1%) to a parallel trending inverse power-law. The general form of this power law is expressed as:

$$\frac{\bar{s}}{s_0} = k\left(\frac{\dot{\varepsilon}}{\dot{\varepsilon}_0}\right)^{-\mu} \tag{9}$$

We fit the data for non-porous and porous rocks using non-linear least squares fitting in log-log space to determine that, for non-porous rocks, the exponent, μ, is 1.93 ± 0.14, and the constant k is $12.2^{+1.93}_{-1.67}$. The power law for porous rocks has an exponent, μ, of 1.78 ± 0.40, and a constant, k, of $0.13^{+0.07}_{-0.04}$ (Table 5). The exponents, μ, for non-porous and porous rocks are within 1σ uncertainty of each other; we emphasise that this exponent relates the strain rate to the median fragment size from mass-size distributions, the median from number-size distributions may scale differently. The constants, k, for the non-porous and porous relationships are significantly different, indicating that the constant is likely to be a function of porosity, or some mechanical or microstructural property closely related to porosity (e.g., flaw density, flaw size, etc.). However, in the absence of a wider variety of tested porous rocks,

Table 4
Literature values of mode-I fracture toughness (K_{IC}).

	Notes	K_{IC} (MPa $m^{1/2}$)
Sandstone	Average of critical K_{IC} values from Atkinson and Meredith (1987) (n = 6)	1.08 ± 0.85
Quartzite	Average of critical K_{IC} values from Atkinson and Meredith (1987) (n = 3)	1.68 ± 0.39
Limestone	Average of critical K_{IC} values from Atkinson and Meredith (1987) (n = 5)	1.11 ± 0.33
Carrara Marble	Atkinson (1979) and Meredith et al. (1984)	0.76 ± 0.16
Granite	Average of critical K_{IC} values from Atkinson and Meredith (1987) (n = 63). Used in Rae et al. (2020)	1.73 ± 0.59
Gneiss (Parallel Foliation)	Used in Rae et al. (2020)	1.56 ± 0.53
Gneiss (Perpendicular Foliation)	Used in Rae et al. (2020)	1.90 ± 0.65

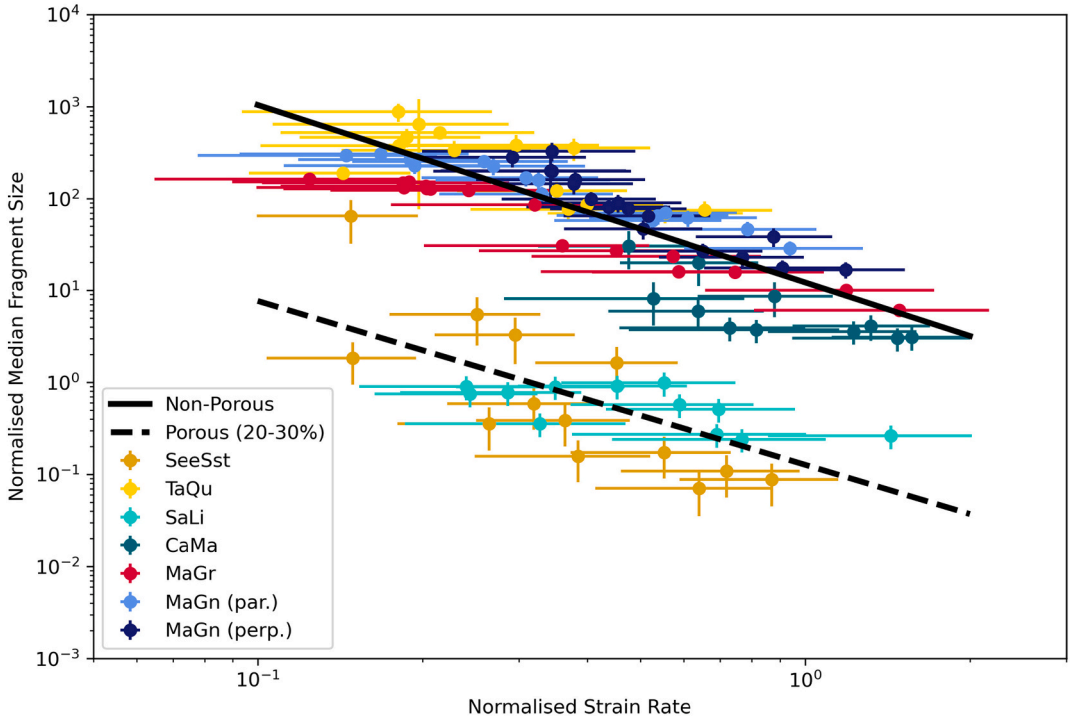

Fig. 7. Scaled empirical fragmentation relationships for non-porous and porous rocks. Non-porous rocks are Taunus Quartzite (TaQu), Carrara Marble (CaMa), and the felsic crystalline rocks presented in (Rae et al., 2020); Malsburg Granite (MaGr) and Maggia Gneiss (MaGn; where the foliation was oriented parallel and perpendicular to the axis of compression). Porous rocks are Seeberger Sandstone (SeeSst) and Savonnières Limestone (SaLi).

Table 5
Empirical fragmentation relationship parameters.

	k	μ
Non-Porous Rocks	$12.2^{+1.93}_{-1.67}$	**1.93 ± 0.14**
Porous Rocks (~20–30%)	$0.13^{+0.07}_{-0.04}$	**1.78 ± 0.40**

we are unable to speculate further on the nature of the dependency of k on porosity. Our relationship for porous rocks is only appropriate for porosities between ~20–30%; less porous rocks are likely to follow trends with intermediate values of k.

4.2.2. *Fragment shapes*

Our results demonstrate that fragment shape is independent of both strain rate and lithology (Figs. 5 and 6). For all of the lithologies in this study, average fragment circularity and axial ratios at all strain rates are both ~0.6. Our results therefore suggest that fragment shape cannot be used as a fingerprint for the conditions at which deformation and, more specifically, fragmentation occurred. Nevertheless, we note that our experiments were only conducted under uniaxial compression; it remains to be seen whether fragment shape in dynamic failure is dependent on the state of stress, whether simply confined or under truly triaxial conditions.

To understand why fragment shape may be independent of strain rate during dynamic fragmentation, we consider the geometric fragmentation of a unit area/volume. At low strain rates, an area/volume will be fragmented by a small number of fractures, producing a small number of large fragments. At high strain rates, the area/volume will be fragmented by a large number of fractures, producing a large number of small fragments. The exact distribution of fragment sizes is fundamentally linked to the method by which fractures are constructed (Grady and Kipp, 1985). Here, we implement a variety of construction algorithms to randomly fragment a two-dimensional area with the aim of seeing how fragment shape changes as a function of the number of fractures (i.e. strain rate). We chose three geometric fragmentation construction algorithms as described by Grady and Kipp (1985): Random Lines, Random Line Segments, and Voronoi Segmentation.

The Random Lines algorithm is the simplest of the three. Here, a specified number of randomly distributed points are placed within a unit area. Each point is then assigned a random orientation (between 0° and 180°), and a fracture (straight line) is extended from that point such that it extends from one edge of the unit area to another, passing through the point at the assigned orientation. This process is conducted for all points simultaneously. The Random Line Segments algorithm has several similarities to the Random Lines algorithm but is more complex, and realistic. Here, each fracture is added sequentially with the condition that the fracture must terminate against any pre-existing fracture. Voronoi segmentation is conceptually rather different to the previous algorithms but also produces random fragmentation of a unit area. Here, a specified number of random points ("seeds") are chosen, and the unit area is divided into segments which contain all of the locations closest to a single seed. For each algorithm, 10 images were generated, each with varying numbers of lines or seeds. Those images were then analysed to characterise the shapes (circularity, C, and axial ratio, AR; **Eqs. 4 and 5**) of the fragments, excluding those at the edge of the unit area, as a function of the number of lines/seeds.

With the Random Lines algorithm, we find that axial ratio is constant as a function of the number of lines while circularity increases (Fig. 8a). With the Random Line Segments and Voronoi algorithms, we found no variation of either circularity or axial ratio with increasing number of lines/seeds (Fig. 8b and c). Of the three algorithms, Voronoi segmentation achieves the closest match to our experimental results with average circularities of ~0.7 and average axial ratios of ~0.6. We emphasise though, that none of the implemented algorithms are particularly representative of the real process of dynamic fragmentation as they ignore all of the physical and dynamic processes of fracture nucleation and growth. Nevertheless, they demonstrate that uniform fragment shapes as a function of strain rate is a consequence of fragmentation as a stochastic process where the growth of fractures is

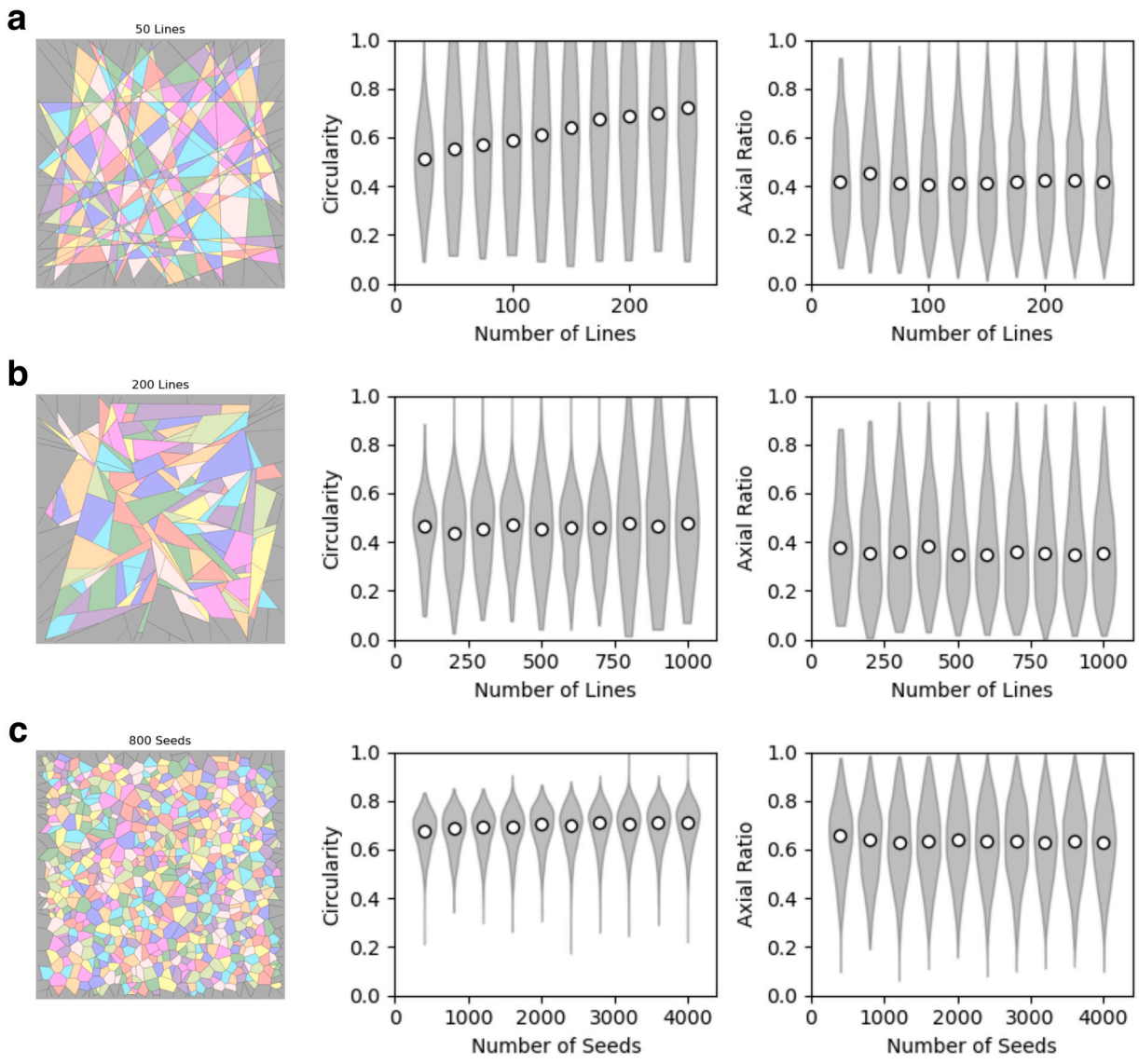

Fig. 8. Examples of geometric fragmentation algorithms and the shapes of fragments as functions of the number of lines/seeds. An increase in the number of lines/seeds is analogous to increasing strain rate, compare with Figs. 5 and 6. a) Random Lines, b) Random Line Segments, c) Voronoi Segmentation.

limited by the presence of other growing fractures. A further implication of our results is that the behaviour of fractures did not change over the conditions explored in our study, i.e. uniaxial compression at rates between ~30 and 300 s^{-1}. Experimental studies have shown that fractures, particularly mode-I fractures, in the dynamic regime may bifurcate or branch under increasing loading rates (Ravi-Chandar and Knauss, 1984b; Zhang and Zhao, 2014; Zhang et al., 1999), this would be expected to lead to the production of more elongate and less circular fragments as a function of increasing rate. However, our results show no variation of fragment shape in common with the simplified geometric models of fragmentation where each fracture behaves the same, regardless of the "strain rate".

4.3. Application to naturally fragmented rocks

Fractured, fragmented, and pulverised rocks commonly occur adjacent to tectonic faults, within landslide deposits, and within impact craters. The results of this study have the potential to be used to constrain loading conditions during deformation events associated with these rocks.

Fragmented and pulverised rocks are most commonly studied in association with tectonic faults. Pulverised rocks have been characterised from a variety of large strike-slip faults; e.g. San Andreas (Rempe et al., 2013; Rockwell et al., 2009; Wechsler et al., 2011; Wilson et al., 2005), Garlock (Rockwell et al., 2009), Atakama (Mitchell and Faulkner, 2009), Arima-Takatsuki (Mitchell et al., 2011), Salzach–Ennstal–Mariazell–Puchberg (SEMP; Schröckenfuchs et al., 2015), Foiana (Fondriest et al., 2015). In general, fragment size and fracture spacing in the damage zone of faults increase with distance from the fault core, nevertheless, individual faults and fault segments have varying minimum fragment sizes. At Tejon Pass on the San Andreas Fault, fragment sizes within 10 m of the fault core are ~25–50 μm, while on the nearby Garlock, fragment sizes are ~75–150 μm (Rockwell et al., 2009). Further along the San Andreas Fault, in the vicinity of Littlerock, average fragment sizes in a drill core ~80 m from the fault core are typically 100–300 μm (Wechsler et al., 2011). In contrast, average fragment sizes in the most heavily pulverised fault rocks on the SEMP and Foiana faults are ~1–30 mm (Fondriest et al., 2015; Schröckenfuchs et al., 2015).

Fragment size analysis of rock avalanche deposits shows considerable spatial variability within deposits (Dufresne and Dunning, 2017; Dunning and Armitage, 2011); nevertheless many deposits have

generally been characterised as possessing inverse grading (e.g., Crosta et al., 2007). In the Val Pola rock avalanche deposits, rock fragments at the surface are ~2–5 m on average while at depths of ~50 m within the deposit, median fragment sizes decrease by a factor ~ 1000 (i.e. ~2–5 mm). Furthermore, fragment size analysis of the Tschirgant and Flims rock avalanche deposits show median fragment sizes between ~1 and ~ 10 mm in "fragmented facies" (Dufresne and Dunning, 2017).

The empirical scaling relationship presented in this study can be directly applied to these results from fault rocks and rock avalanche deposits. If we assume that the affected rocks are non-porous, have a quasi-static uniaxial compressive strength of 100 MPa, mode-I fracture toughness of 1 MPa $m^{-1/2}$, and characteristic strain rate of 250 s^{-1}; then fragment sizes of 1 μm correspond to strain rates of ~9.9×10^3 s^{-1}, 1 mm corresponds to 2.8×10^2 s^{-1}, and 1 m corresponds to 7.7×10^0 s^{-1}. Overall, this suggests that strain rates during rupture events on pulverising faults reach values of at least ~10^2–10^3 s^{-1} while strain rates during rock avalanches reach strain rates of ~10^1–10^2 s^{-1}. For earthquake rupture, these strain rates are broadly consistent with analytical models of strain rates during dynamic rupture (Doan and Gary, 2009; Reches and Dewers, 2005).

Despite the apparent consistency between analytical models of rock deformation and the predicted strain rates from use of the fragment scaling relationship of this study with natural samples, several effects that may have significant consequences have not been considered: the role of confining stresses (and truly triaxial stresses), the effect of pore-fluid pressures, and the effect of repeated failure. Observations indicate that pulverisation in fault rocks ceases beyond 3–4 km depth (Dor et al., 2006b) and experimental results corroborate that confining pressures inhibit the fragmentation of rocks at high strain rates (Liu et al., 2019; Liu and Zhao, 2021; Yuan et al., 2011). Furthermore, it remains to be seen how truly triaxial stress states that would be more representative natural stress states may affect the dynamic behaviour of rocks. An additional concern in the scaling of fragment sizes from porous rocks is the effect of pore fluids and rheologically distinct interstitial material (e.g., Peppard et al., 2018). Finally, the experiments in this study were conducted on intact samples, it is unclear how the fragmentation resulting from a single high-rate deformation event can be differentiated from the effect of repeated moderate rate events (e.g., Aben et al., 2016a).

5. Conclusions

In this study, we have shown that the characteristic strain rates for rate-dependent strength and brittle behaviour under uniaxial compressive loading in sandstone, quartzite, limestone, and marble ranges between ~144–322 s^{-1}. The degree of fragmentation increases with strain rate over the full range of dynamic rates investigated (~30–350 s^{-1}). Our results demonstrate that compressive fragmentation cannot be described by tensile fragmentation models, and instead we describe an empirical fragmentation relationship for uniaxial compression that describes average fragment size as a function of strain rate. This relation has the form of an inverse power-law with an exponent of 1.93 +/− 0.14 and a constant that varies with porosity, or some material property correlated with porosity. The applicability of this relation at strain rates at greater or lesser strain rates remains to be seen. The results of our study also demonstrate that fragment shape during dynamic failure is independent of strain rate and lithology, at least for uniaxial compression and the homogeneous lithologies investigated here.

The clear implication of this study is that fragment size may be used as a diagnostic indicator of the strain rate at failure while fragment shape cannot be used. Nevertheless, we recommend cautious use of our empirical relationship between strain rate and fragment size. Confinement or truly triaxial stress states during fragmentation may cause significant changes to the process of dynamic fragmentation (Liu et al., 2019; Liu and Zhao, 2021; Yuan et al., 2011) and the fragmentation relation described here. Furthermore, our experiments were conducted on intact rocks, it remains unclear how fragments generated by repeated low-rate events (Aben et al., 2016b) can be differentiated from single high-rate events.

Acknowledgments and data availability

The authors wish to acknowledge Herbert Ickler and Gordon Mette for preparation of samples. Tony Kern is thanked for assistance in sample preparation and UCS experiments. Additionally, Sebastian Hess of the Ernst-Mach Institute is thanked for technical assistance with the SHPB. Lennart Fischer is thanked for the instruction and use of the PICAT imaging system. All data presented within this publication can be found in the **Supplementary Online Material** at https://github.com/ASprae/Dynamic-Strength-and-Fragmentation. This work was funded by DFG Project KE 732/27–1. The authors gratefully acknowledge the constructive and thoughtful comments of two anonymous reviewers and the editor, Phillipe Agard.

Declaration of Competing Interest

The authors declare that they have no known competing financial interests or personal relationships that could have appeared to influence the work reported in this paper.

Appendix A. Supplementary data

Supplementary data to this article can be found online at https://doi.org/10.1016/j.tecto.2022.229221.

References

Aben, F.M., Doan, M.-L., Mitchell, T.M., Toussaint, R., Reuschlé, T., Fondriest, M., Gratier, J.-P., Renard, F., 2016a. Dynamic fracturing by successive coseismic loadings leads to pulverization in active fault zones. J. Geophys. Res. Solid Earth 121, 2338–2360. https://doi.org/10.1002/2015JB012542.

Aben, F.M., Doan, M.-L., Mitchell, T.M., Toussaint, R., Reuschlé, T., Fondriest, M., Gratier, J.-P., Renard, F., 2016b. Dynamic fracturing by successive coseismic loadings leads to pulverization in active fault zones. J. Geophys. Res. Solid Earth 121, 2338–2360. https://doi.org/10.1002/2015JB012542.

Aben, F.M., Doan, M.-L., Gratier, J.-P., Renard, F., 2017. Coseismic damage Generation and pulverization in fault zones. In: Fault Zone Dynamic Processes. American Geophysical Union (AGU), pp. 47–80. https://doi.org/10.1002/9781119156895.ch4.

Agosta, F., Aydin, A., 2006. Architecture and deformation mechanism of a basin-bounding normal fault in Mesozoic platform carbonates, Central Italy. J. Struct. Geol. 28, 1445–1467. https://doi.org/10.1016/j.jsg.2006.04.006.

Alam, Md.S., Chakraborty, T., Matsagar, V., Rao, K.S., Sharma, P., Singh, M., 2015. Characterization of Kota Sandstone under Different Strain rates in Uniaxial Loading. Geotech. Geol. Eng. 33, 143–152. https://doi.org/10.1007/s10706-014-9810-3.

Atkinson, B.K., 1979. Fracture toughness of Tennessee Sandstone and Carrara Marble using the double torsion testing method. Int. J. Rock Mech. Min. Sci. Geomech. Abstr. 16, 49–53. https://doi.org/10.1016/0148-9062(79)90774-5.

Atkinson, B.K., Meredith, P.G., 1987. Experimental fracture mechanics data for rocks and minerals. In: Atkinson, B.K. (Ed.), Fracture Mechanics of Rock. Academic Press, London, pp. 477–525.

Barber, T., Griffith, W.A., 2017. Experimental constraints on dynamic fragmentation as a dissipative process during seismic slip. Philos. Trans. R. Soc. A Math. Phys. Eng. Sci. 375, 20160002. https://doi.org/10.1098/rsta.2016.0002.

Bhat, H.S., Rosakis, A.J., Sammis, C.G., 2012. A Micromechanics based constitutive model for brittle failure at high strain rates. J. Appl. Mech. 79 https://doi.org/10.1115/1.4005897.

Blanton, T.L., 1981. Effect of strain rates from 10-2 to 10 sec-1 in triaxial compression tests on three rocks. Int. J. Rock Mech. Min. Sci. Geomech. Abstr. 18, 47–62. https://doi.org/10.1016/0148-9062(81)90265-5.

Brune, J.N., Brown, S., Johnson, P.A., 1993. Rupture mechanism and interface separation in foam rubber models of earthquakes: a possible solution to the heat flow paradox and the paradox of large overthrusts. Tectonophysics, New Horiz. Strong Motion: Seismic Stud. Eng. Pract. 218, 59–67. https://doi.org/10.1016/0040-1951(93)90259-M.

Camacho, G.T., Ortiz, M., 1996. Computational modelling of impact damage in brittle materials. Int. J. Solids Struct. 33, 2899–2938. https://doi.org/10.1016/0020-7683(95)00255-3.

Chen, W.W., Song, B., 2010. Split Hopkinson (Kolsky) Bar: Design. Springer Science & Business Media, Testing and Applications.

Crosta, G.B., Frattini, P., Fusi, N., 2007. Fragmentation in the Val Pola rock avalanche, Italian Alps. J. Geophys. Res. Earth Surf. 112 https://doi.org/10.1029/2005JF000455.

De Blasio, F.V., Crosta, G.B., 2014. Simple physical model for the fragmentation of rock avalanches. Acta Mech. 225, 243–252. https://doi.org/10.1007/s00707-013-0942-y.
Doan, M.-L., Billi, A., 2011. High strain rate damage of Carrara marble. Geophys. Res. Lett. 38 https://doi.org/10.1029/2011GL049169.
Doan, M.-L., d'Hour, V., 2012. Effect of initial damage on rock pulverization along faults. J. Struct. Geol. Fault Zone Structure, Mech. Evol. Nat. Exp. 45, 113–124. https://doi.org/10.1016/j.jsg.2012.05.006.
Doan, M.-L., Gary, G., 2009. Rock pulverization at high strain rate near the San Andreas fault. Nat. Geosci. 2, 709–712. https://doi.org/10.1038/ngeo640.
Dor, O., Ben-Zion, Y., Rockwell, T.K., Brune, J., 2006a. Pulverized rocks in the Mojave section of the San Andreas Fault Zone. Earth Planet. Sci. Lett. 245, 642–654. https://doi.org/10.1016/j.epsl.2006.03.034.
Dor, O., Rockwell, T.K., Ben-Zion, Y., 2006b. Geological observations of damage asymmetry in the structure of the San Jacinto, San Andreas and Punchbowl Faults in Southern California: a possible indicator for preferred rupture propagation direction. Pure Appl. Geophys. 163, 301–349. https://doi.org/10.1007/s00024-005-0023-9.
Drugan, W.J., 2001. Dynamic fragmentation of brittle materials: analytical mechanics-based models. J. Mech. Physics Solids 49, 1181–1208. https://doi.org/10.1016/S0022-5096(01)00002-3.
Dufresne, A., Dunning, S.A., 2017. Process dependence of grain size distributions in rock avalanche deposits. Landslides 14, 1555–1563. https://doi.org/10.1007/s10346-017-0806-y.
Dunning, S.A., Armitage, P.J., 2011. The Grain-size distribution of rock-avalanche deposits: implications for natural dam stability. In: Evans, S.G., Hermanns, R.L., Strom, A., Scarascia-Mugnozza, G. (Eds.), Natural and Artificial Rockslide Dams, Lecture Notes in Earth Sciences. Springer, Berlin, Heidelberg, pp. 479–498. https://doi.org/10.1007/978-3-642-04764-0_19.
Ebert, M., Hecht, L., Deutsch, A., Kenkmann, T., Wirth, R., Berndt, J., 2014. Geochemical processes between steel projectiles and silica-rich targets in hypervelocity impact experiments. Geochim. Cosmochim. Acta 133, 257–279. https://doi.org/10.1016/j.gca.2014.02.034.
Faulkner, D.R., Lewis, A.C., Rutter, E.H., 2003. On the internal structure and mechanics of large strike-slip fault zones: field observations of the Carboneras fault in southeastern Spain. Tectonophysics 367, 235–251. https://doi.org/10.1016/S0040-1951(03)00134-3.
Fineberg, J., Gross, S.P., Marder, M., Swinney, H.L., 1991. Instability in dynamic fracture. Phys. Rev. Lett. 67, 457–460. https://doi.org/10.1103/PhysRevLett.67.457.
Fondriest, M., Aretusini, S., Di Toro, G., Smith, S.A.F., 2015. Fracturing and rock pulverization along an exhumed seismogenic fault zone in dolostones: the Foiana Fault Zone (Southern Alps, Italy). Tectonophysics 654, 56–74. https://doi.org/10.1016/j.tecto.2015.04.015.
Fondriest, M., Doan, M.-L., Aben, F., Fusseis, F., Mitchell, T.M., Voorn, M., Secco, M., Di Toro, G., 2017. Static versus dynamic fracturing in shallow carbonate fault zones. Earth Planet. Sci. Lett. 461, 8–19. https://doi.org/10.1016/j.epsl.2016.12.024.
Fredrich, J.T., Evans, B., Wong, T.-F., 1989. Micromechanics of the brittle to plastic transition in Carrara marble. J. Geophys. Res. Solid Earth 94, 4129–4145. https://doi.org/10.1029/JB094iB04p04129.
Frew, D.J., Forrestal, M.J., Chen, W., 2001. A split Hopkinson pressure bar technique to determine compressive stress-strain data for rock materials. Exp. Mech. 41, 40–46. https://doi.org/10.1007/BF02323102.
Ghaffari, H.O., Griffith, W.A., Barber, T.J., 2019. Energy delocalization during dynamic rock fragmentation. Geophys. J. Int. 217, 1034–1046. https://doi.org/10.1093/gji/ggz064.
Glenn, L.A., Chudnovsky, A., 1986. Strain-energy effects on dynamic fragmentation. J. Appl. Phys. 59, 1379–1380. https://doi.org/10.1063/1.336532.
Grady, D.E., 1982. Local inertial effects in dynamic fragmentation. J. Appl. Phys. 53, 322–325. https://doi.org/10.1063/1.329934.
Grady, D., 2007. Fragmentation of Rings and Shells: The Legacy of N.F. Mott. Springer Science & Business Media.
Grady, D., 2009. Dynamic fragmentation of solids. In: Shock Wave Science and Technology Reference Library, Vol. 3. Solids II. Springer, Berlin, Heidelberg, pp. 169–276. https://doi.org/10.1007/978-3-540-77080-0_4.
Grady, D.E., 2010. Length scales and size distributions in dynamic fragmentation. Int. J. Fract. 163, 85–99. https://doi.org/10.1007/s10704-009-9418-4.
Grady, D.E., Kipp, M.E., 1985. Geometric statistics and dynamic fragmentation. J. Appl. Phys. 58, 1210–1222. https://doi.org/10.1063/1.336139.
Green, S.J., Leasia, J.D., Perkins, R.D., Jones, A.H., 1972. Triaxial stress behavior of Solenhofen limestone and westerly granite at high strain rates. J. Geophys. Res. 1896-1977 (77), 3711–3724. https://doi.org/10.1029/JB077i020p03711.
Hawkes, I., Mellor, M., 1970. Uniaxial testing in rock mechanics laboratories. Eng. Geol. 4, 179–285. https://doi.org/10.1016/0013-7952(70)90034-7.
Hawkins, A.B., 1998. Aspects of rock strength. Bull. Eng. Geol. Environ. 57, 17–30. https://doi.org/10.1007/s100640050017.
Heilbronner, R., Barrett, S., 2014. Image analysis in Earth sciences: microstructures and textures of Earth materials, Springer-Verlag, Berlin Heidelberg. https://doi.org/10.1007/978-3-642-10343-8.
Hild, F., Forquin, P., da Silva, A.R.C., 2003. Single and multiple fragmentation of brittle geomaterials. Revue Française de Génie Civil 7, 973–1002. https://doi.org/10.1080/12795119.2003.9692529.
Hogan, J.D., Rogers, R.J., Spray, J.G., Boonsue, S., 2012. Dynamic fragmentation of granite for impact energies of 6–28J. Eng. Fract. Mech. 79, 103–125. https://doi.org/10.1016/j.engfracmech.2011.10.006.
Hogan, J.D., Castillo, J.A., Rawle, A., Spray, J.G., Rogers, R.J., 2013. Automated microscopy and particle size analysis of dynamic fragmentation in natural ceramics. Eng. Fract. Mech. 98, 80–91. https://doi.org/10.1016/j.engfracmech.2012.11.021.
Hogan, J.D., Farbaniec, L., Daphalapurkar, N., Ramesh, K.T., 2016. On compressive brittle fragmentation. J. Am. Ceram. Soc. 99, 2159–2169. https://doi.org/10.1111/jace.14171.
Housen, K.R., Holsapple, K.A., 1999. Scale effects in strength-dominated collisions of rocky asteroids. Icarus 142, 21–33. https://doi.org/10.1006/icar.1999.6206.
Howe, S.P., Goldsmith, W., Sackman, J.L., 1974. Macroscopic static and dynamic mechanical properties of Yule marble. Exp. Mech. 14, 337–346. https://doi.org/10.1007/BF02323559.
Jaeger, J.C., Cook, N.G.W., Zimmerman, R., 2007. Fundamentals of Rock Mechanics. Blackwell Publishing.
Kenkmann, T., Poelchau, M.H., Wulf, G., 2014. Structural geology of impact craters. J. Struct. Geol. 62, 156–182. https://doi.org/10.1016/j.jsg.2014.01.015.
Key, W.R.O., Schultz, R.A., 2011. Fault formation in porous sedimentary rocks at high strain rates: first results from the Upheaval Dome impact structure, Utah, USA. GSA Bull. 123, 1161–1170. https://doi.org/10.1130/B30087.1.
Kimberley, J., Ramesh, K.T., Daphalapurkar, N.P., 2013. A scaling law for the dynamic strength of brittle solids. Acta Mater. 61, 3509–3521. https://doi.org/10.1016/j.actamat.2013.02.045.
Lankford, J., Blanchard, C.R., 1991. Fragmentation of brittle materials at high rates of loading. J. Mater. Sci. 26, 3067–3072. https://doi.org/10.1007/BF01124844.
Levy, S., Molinari, J.F., 2010. Dynamic fragmentation of ceramics, signature of defects and scaling of fragment sizes. J. Mech. Physics Solids 58, 12–26. https://doi.org/10.1016/j.jmps.2009.09.002.
Li, X.F., Li, H.B., Zhang, Q.B., Jiang, J.L., Zhao, J., 2018. Dynamic fragmentation of rock material: characteristic size, fragment distribution and pulverization law. Eng. Fract. Mech. 199, 739–759. https://doi.org/10.1016/j.engfracmech.2018.06.024.
Liu, K., Zhao, J., 2021. Progressive damage behaviours of triaxially confined rocks under multiple dynamic loads. Rock Mech. Rock. Eng. 54, 3327–3358. https://doi.org/10.1007/s00603-021-02408-z.
Liu, J.-Z., Xu, J.-Y., Lv, X.-C., Zhao, D.-H., Leng, B.-L., 2012. Experimental study on dynamic mechanical properties of amphibolites, sericite-quartz schist and sandstone under impact loadings. Int. J. Nonlin. Sci. Num. Simul. 13, 209–217. https://doi.org/10.1515/ijnsns.2011.121.
Liu, K., Zhang, Q.B., Wu, G., Li, J.C., Zhao, J., 2019. Dynamic mechanical and fracture behaviour of sandstone under multiaxial loads using a triaxial Hopkinson bar. Rock Mech. Rock. Eng. 52, 2175–2195. https://doi.org/10.1007/s00603-018-1691-y.
Meredith, P.G., Atkinson, B.K., Hillmann, N.B., 1984. Progress in experimental petrology. In: 6th Report. NERC Pubs. Ser. D. No. 25, Swindon, UK.
Millon, O., Ruiz-Ripoll, M.L., Hoerth, T., 2016. Analysis of the behavior of sedimentary rocks under impact loading. Rock Mech. Rock. Eng. 49, 4257–4272. https://doi.org/10.1007/s00603-016-1010-4.
Mitchell, T.M., Faulkner, D.R., 2009. The nature and origin of off-fault damage surrounding strike-slip fault zones with a wide range of displacements: a field study from the Atacama fault system, northern Chile. J. Struct. Geol. 31, 802–816. https://doi.org/10.1016/j.jsg.2009.05.002.
Mitchell, T.M., Ben-Zion, Y., Shimamoto, T., 2011. Pulverized fault rocks and damage asymmetry along the Arima-Takatsuki Tectonic Line, Japan. Earth Planet. Sci. Lett. 308, 284–297. https://doi.org/10.1016/j.epsl.2011.04.023.
Paliwal, B., Ramesh, K.T., 2008. An interacting micro-crack damage model for failure of brittle materials under compression. J. Mech. Physics Solids 56, 896–923. https://doi.org/10.1016/j.jmps.2007.06.012.
Peppard, D.W., Webb, H.N., Dennis, K., Vierra, E., Girty, G.H., Rockwell, T.K., Blanton, C.M., Brown, J.F., Goldstein, A.I., Kastama, K.W., Korte-Nahabedian, M.A., Puckett, D., Richter, A.K., 2018. Micro-scale damage characterized within part of a dismembered positive flower structure, San Jacinto fault, southern California, USA. J. Struct. Geol. 112, 53–68. https://doi.org/10.1016/j.jsg.2018.04.014.
Pieri, M., Burlini, L., Kunze, K., Stretton, I., Olgaard, D.L., 2001. Rheological and microstructural evolution of Carrara marble with high shear strain: results from high temperature torsion experiments. J. Struct. Geol. 23, 1393–1413. https://doi.org/10.1016/S0191-8141(01)00006-2.
Poelchau, M.H., Kenkmann, T., Hoerth, T., Schäfer, F., Rudolf, M., Thoma, K., 2014. Impact cratering experiments into quartzite, sandstone and tuff: the effects of projectile size and target properties on spallation. Icarus 242, 211–224. https://doi.org/10.1016/j.icarus.2014.08.018.
Rae, A.S.P., Kenkmann, T., Padmanabha, V., Poelchau, M.H., Schäfer, F., 2020. Dynamic Compressive Strength and Fragmentation in Felsic Crystalline Rocks. J. Geophys. Res.: Planets 125. https://doi.org/10.1029/2020JE006561 e2020JE006561.
Ramesh, K.T., Hogan, J.D., Kimberley, J., Stickle, A., 2015. A review of mechanisms and models for dynamic failure, strength, and fragmentation. Planetary and Space Science, VIII Workshop on Catastrophic Disruption in the Solar System 107, 10–23. https://doi.org/10.1016/j.pss.2014.11.010.
Ravi-Chandar, K., Knauss, W.G., 1984a. An experimental investigation into dynamic fracture: I. Crack initiation and arrest. Int. J. Fract. 25, 247–262. https://doi.org/10.1007/BF00963460.
Ravi-Chandar, K., Knauss, W.G., 1984b. An experimental investigation into dynamic fracture: II. Microstructural aspects. Int. J. Fract. 26, 65–80. https://doi.org/10.1007/BF01152313.
Reches, Z., Dewers, T.A., 2005. Gouge formation by dynamic pulverization during earthquake rupture. Earth Planet. Sci. Lett. 235, 361–374. https://doi.org/10.1016/j.epsl.2005.04.009 10.1016/j.epsl.2005.04.009.
Rempe, M., Mitchell, T., Renner, J., Nippress, S., Ben-Zion, Y., Rockwell, T., 2013. Damage and seismic velocity structure of pulverized rocks near the San Andreas

Fault. J. Geophys. Res. Solid Earth 118, 2813–2831. https://doi.org/10.1002/jgrb.50184.
Rockwell, T., Sisk, M., Girty, G., Dor, O., Wechsler, N., Ben-Zion, Y., 2009. Chemical and physical characteristics of pulverized tejon lookout granite adjacent to the San Andreas and Garlock faults: implications for earthquake physics. Pure Appl. Geophys. 166, 1725–1746. https://doi.org/10.1007/s00024-009-0514-1.
Rosakis, A.J., 1999. Explosion at the Parthenon: Can We Pick Up the Pieces? (Technical Report No. 99–3). GALCIT SM.
Rowe, C.D., Griffith, W.A., 2015. Do faults preserve a record of seismic slip: a second opinion. J. Struct. Geol. 78, 1–26. https://doi.org/10.1016/j.jsg.2015.06.006.
Sagy, A., Korngreen, D., 2012. Dynamic branched fractures in pulverized rocks from a deep borehole. Geology 40, 799–802. https://doi.org/10.1130/G33194.1.
Schindelin, J., Arganda-Carreras, I., Frise, E., Kaynig, V., Longair, M., Pietzsch, T., Preibisch, S., Rueden, C., Saalfeld, S., Schmid, B., Tinevez, J.-Y., White, D.J., Hartenstein, V., Eliceiri, K., Tomancak, P., Cardona, A., 2012. Fiji: an open-source platform for biological-image analysis. Nat. Methods 9, 676–682. https://doi.org/10.1038/nmeth.2019.
Schröckenfuchs, T., Bauer, H., Grasemann, B., Decker, K., 2015. Rock pulverization and localization of a strike-slip fault zone in dolomite rocks (Salzach–Ennstal–Mariazell–Puchberg fault, Austria). J. Struct. Geol. 78, 67–85. https://doi.org/10.1016/j.jsg.2015.06.009.
Sharon, E., Fineberg, J., 1999. Confirming the continuum theory of dynamic brittle fracture for fast cracks. Nature 397, 333–335. https://doi.org/10.1038/16891.
Van Stappen, J.F., De Kock, T., De Schutter, G., Cnudde, V., 2019. Uniaxial compressive strength measurements of limestone plugs and cores: a size comparison and X-ray CT study. Bull. Eng. Geol. Environ. 78, 5301–5310. https://doi.org/10.1007/s10064-018-01448-0.
Wang, H., Ramesh, K.T., 2004. Dynamic strength and fragmentation of hot-pressed silicon carbide under uniaxial compression. Acta Mater. 52, 355–367. https://doi.org/10.1016/j.actamat.2003.09.036.
Wechsler, N., Allen, E.E., Rockwell, T.K., Girty, G., Chester, J.S., Ben-Zion, Y., 2011. Characterization of pulverized granitoids in a shallow core along the San Andreas Fault, Littlerock, CA. Geophys. J. Int. 186, 401–417. https://doi.org/10.1111/j.1365-246X.2011.05059.x.
Wilson, B., Dewers, T., Reches, Z., Brune, J., 2005. Particle size and energetics of gouge from earthquake rupture zones. Nature 434, 749–752. https://doi.org/10.1038/nature03433.
Xia, K., Yao, W., 2015. Dynamic rock tests using split Hopkinson (Kolsky) bar system – a review. J. Rock Mech. Geotech. Eng. 7, 27–59. https://doi.org/10.1016/j.jrmge.2014.07.008.
Yao, W., Xu, Y., Xia, K., 2020. Damage evolution during rock pulverization induced by dynamic compressive loading. J. Geophys. Res. Solid Earth 125. https://doi.org/10.1029/2020JB019388 e2020JB019388.
Yuan, F., Prakash, V., Tullis, T., 2011. Origin of pulverized rocks during earthquake fault rupture. J. Geophys. Res. Solid Earth 116. https://doi.org/10.1029/2010JB007721.
Zhang, Q.B., Zhao, J., 2014. A review of dynamic experimental techniques and mechanical behaviour of rock materials. Rock Mech. Rock. Eng. 47, 1411–1478. https://doi.org/10.1007/s00603-013-0463-y.
Zhang, Z.X., Kou, S.Q., Yu, J., Yu, Y., Jiang, L.G., Lindqvist, P.-A., 1999. Effects of loading rate on rock fracture. Int. J. Rock Mech. Min. Sci. 36, 597–611. https://doi.org/10.1016/S0148-9062(99)00031-5.
Zhou, F., Molinari, J.-F., Ramesh, K.T., 2006a. Analysis of the brittle fragmentation of an expanding ring. Computational Materials Science, Proceedings of the 14th International Workshop on Computational Mechanics of Materials 37, 74–85. https://doi.org/10.1016/j.commatsci.2005.12.017.
Zhou, F., Molinari, J.-F., Ramesh, K.T., 2006b. Effects of material properties on the fragmentation of brittle materials. Int. J. Fract. 139, 169–196. https://doi.org/10.1007/s10704-006-7135-9.
Zhou, Y.X., Xia, K., Li, X.B., Li, H.B., Ma, G.W., Zhao, J., Zhou, Z.L., Dai, F., 2011. Suggested Methods for determining the Dynamic Strength Parameters and Mode-I Fracture Toughness of Rock Materials. In: Ulusay, R. (Ed.), The ISRM Suggested Methods for Rock Characterization, Testing and Monitoring: 2007–2014. Springer International Publishing, Cham, pp. 35–44. https://doi.org/10.1007/978-3-319-07713-0_3.
Zou, C., Wong, L.N.Y., 2016. Size and geometry effects on the mechanical properties of Carrara marble under dynamic loadings. Rock Mech. Rock. Eng. 49, 1695–1708. https://doi.org/10.1007/s00603-015-0899-3.
Zwiessler, R., Kenkmann, T., Poelchau, M.H., Nau, S., Hess, S., 2017. On the use of a split Hopkinson pressure bar in structural geology: High strain rate deformation of Seeberger sandstone and Carrara marble under uniaxial compression. J. Struct. Geol. 97, 225–236. https://doi.org/10.1016/j.jsg.2017.03.007.